Geophysical Journal International

Geophys. J. Int. (2026) **245,** 1–22
Advance Access publication 2026 February 05
Research Paper

https://doi.org/10.1093/gji/ggag058

Single and multi-objective optimization of distributed acoustic sensing cable layouts for geophysical applications

Dominik Strutz [1], Tjeerd Kiers[2] and Andrew Curtis[1]

[1]*School of Geosciences, University of Edinburgh, Edinburgh EH93FE, UK. E-mail: dominik.strutz@ed.ac.uk*
[2]*Institute of Geophysics, ETH Zurich, CH-8092 Zurich, Switzerland*

Accepted 2026 February 1. Received 2026 January 6; in original form 2025 October 3

SUMMARY

We present a systematic approach to optimize distributed acoustic sensing (DAS) fibre-optic cable layouts using global optimization techniques. Our method represents cable geometries using splines, enabling efficient exploration of layouts while respecting physical deployment constraints. The use of evolutionary algorithms enables single and multi-objective optimization, taking into account complex design constraints such as terrain, accessibility, exclusion zones, cable length and coupling-related or local site effects, while allowing efficient parallelization of the optimization process. We demonstrate the approach on a real-world case study, optimizing the layout of a DAS cable for monitoring slope stability in the Cuolm da Vi area of Switzerland. We adapt design criteria for seismic source location problems, and for ambient noise surface wave tomography, to account for the unique characteristics of DAS, such as directional sensitivity patterns. The results show significant potential for improvements in source location accuracy and surface wave tomographic resolution by optimizing cable layouts, highlighting the potential of this approach for optimizing DAS deployments in various geophysical applications.

Key words: Statistical methods; Distributed acoustic sensing; Earthquake monitoring and test-ban treaty verification; Seismic tomography.

1 INTRODUCTION

Distributed acoustic sensing (DAS) has expanded observational capabilities in various seismological applications, including subsurface tomography (e.g. T.M. Daley *et al.* 2013, 2016), reservoir monitoring (e.g. A. Mateeva *et al.* 2014), volcanology (e.g. S. Klaasen *et al.* 2021; A. Fichtner *et al.* 2022; P. Jousset *et al.* 2022), glaciology (e.g. F. Walter *et al.* 2020; T.S. Hudson *et al.* 2021), earthquake-induced ground motion analysis (e.g. Z.J. Spica *et al.* 2020; Y. Yang *et al.* 2022) and seismic event detection and monitoring (e.g. E.R. Martin *et al.* 2017; N.J. Lindsey *et al.* 2017; S. Thrastarson *et al.* 2021; S. Baba *et al.* 2024; A.F. Baird *et al.* 2025; T.S. Hudson *et al.* 2025; Y. Miao *et al.* 2025).

Compared to traditional individual seismic sensors, DAS offers several advantages such as high spatial density, and the ability to deploy sensing elements over long distances without the need for power at the points where data are recorded. These benefits make DAS particularly suitable for the creation of dense arrays, in environmentally sensitive or seafloor deployments and in remote or hazardous environments. However, the sensitivity of DAS cables poses a challenge for optimal cable placement, as the channels exhibit more extreme, directionally anisotropic sensitivity patterns to waves incident on the fibre than single-component geophones (B.N. Kuvshinov 2016; E.R. Martin *et al.* 2017). This directional sensitivity can lead to suboptimal data acquisition if the cable layout is not designed carefully.

Despite many studies on experimental design for geophysical applications such as source location and tomography (e.g. N. Rabinowitz & D.M. Steinberg 1990; D.M. Steinberg *et al.* 1995; H. Maurer & D.E. Boerner 1998; A. Curtis 1999a, b; A. Curtis *et al.* 2004; A. Curtis 2004a, b; H. Maurer *et al.* 2010; H. Bloem *et al.* 2020; V. Krampe *et al.* 2021; D. Strutz & A. Curtis 2024; J. Callahan *et al.* 2025) and advances in design optimization methodology (e.g. A. Foster *et al.* 2019; S. Kleinegesse & M.U. Gutmann 2021; A. Mercier *et al.* 2025), there remains a lack of systematic approaches for optimizing DAS cable layouts. The Kangerlussuaq algorithm proposed by A. Fichtner & C. Hofstede (2022) is a notable exception: while it does not account for the directional sensitivity of DAS cables and cannot be readily extended to multiple design criteria, it locally perturbs an initial cable layout to find designs that improve a given design criterion. The work of both S.P. Näsholm *et al.* (2022) and T. Luckie & R. Porritt (2024) focuses on the effect of cable directionality on the performance of a small number of chosen layouts, but does not provide a systematic approach to optimize the cable.

Table 1. Table of symbols.

Symbol	Definition
N_{cha}	Number of channels
$\mathbf{c}_i$	Location of channel i
$\mathbf{u}_i$	Unit vector defining the orientation of the cable at channel i
$\mathcal{L}$	Cable layout defined by channel locations and orientations
N_{knot}	Number of knots
$\mathbf{k}_i$	Knot location i
R_{ref}	Reference distance for signal-to-noise ratio normalization
ξ	Strain rate sensitivity
φ	Incidence angle of the seismic wave
θ	Azimuth of the channel relative to wave propagation direction
A_{meas}	Amplitude measured by the DAS cable
A_{wave}	Amplitude of the incident seismic wave
$A_i^{\text{P}}, A_i^{\text{S}}$	Peak amplitude of DAS strain rate for P and S waves
$K_i^{\text{P}}, K_i^{\text{S}}$	Channel-specific factors in magnitude scale

We present a systematic global optimization approach to design DAS cable layouts for any number of design criteria, while ensuring the avoidance of obstacles or precluded areas. We demonstrate the optimization process using two criteria: optimizing the cable layout for (1) linearized surface wave tomography, and (2) probabilistic seismic source location, both of which are adapted to account for the directional sensitivity of DAS cables. We therefore cover two common seismological applications, and also the two main approaches to design experiments: computationally efficient linearized experimental design that can scale to large problems, and fully Bayesian experimental design that accounts for the full nonlinearity of the problem, but typically comes at a higher computational cost. The real-world applicability of the proposed method is demonstrated by optimizing a DAS cable layout for different scenarios on the Cuolm da Vi slope instability.

2 METHODS

Table of symbols

This work incorporates concepts from distributed acoustic sensing, seismology, linearized and fully nonlinear Bayesian experimental design, and global optimization. We now introduce the relevant methodology and how it applies to the optimization of DAS cable layouts. Given the potentially broad scope of each of these multiple topics, we keep the introductions relatively brief and refer to the literature for more detailed treatments. The symbols used for the general parametrization of DAS cables and the description of signal decay and sensitivity are summarised in Table 1.

2.1 Distributed acoustic sensing

Distributed acoustic sensing (DAS) transforms standard fibre-optic cables into dense arrays of seismic sensors by measuring strain rate along the cable (N.J. Lindsey & E.R. Martin 2021). It operates by firing a laser pulse through one end of the cable and detecting temporally varying phase shifts in laser light backscattered by Rayleigh scattering at fibre impurities, where the variations are assumed to be caused mainly by strain along the cable axis. These measurements are averaged over a user-defined gauge length, which represents the spatial resolution of the system and determines the length of fibre over which strain rate is averaged to obtain each recorded signal (J.B. Ajo-Franklin *et al.* 2019; N.J. Lindsey & E.R. Martin 2021). The locations at which these averaged ('distributed') strain rates are recorded are referred to as channels, and the distance between these channels is referred to as channel spacing.

For the purpose of this study, we assume that the fibre-optic cable on which DAS is performed consists of a sequence of channels, each with a location and orientation. We treat the recorded data as point measurements located at the centre of each channel. Channel locations are denoted by $\{\mathbf{c}_i\}_{i=1}^{N_{\text{cha}}}$ and the orientation of the cable at channel i is given by the unit vectors $\{\mathbf{u}_i\}_{i=1}^{N_{\text{cha}}}$, where N_{cha} is the number of channels. A cable layout is then represented by the set of channel locations and orientations $\mathcal{L} = \{\mathbf{c}_i, \mathbf{u}_i\}_{i=1}^{N_{\text{cha}}}$.

The main design constraint for a DAS cable layout compared to a conventional seismic survey is that the channels follow a continuous path. To achieve this, we parametrize the cable path using knot locations $\{\mathbf{k}_i\}_{i=1}^{N_{\text{knot}}}$, where N_{knot} is the number of knots. We can use these knots to define a continuous path by interpolation between the knots with a spline function. In this study we use B-splines (C. De Boor 2001; P. Virtanen *et al.* 2020) of a given degree k, but other algorithms that construct a continuous path from a set of knots could be used equally well.

Once the spline has been constructed, we can interpolate the channel locations $\mathbf{c}_i$ along the spline at any desired (here, constant) channel spacing. The knot locations and channel spacing therefore define the number of channels N_{cha}. We can then calculate the channel orientations $\mathbf{u}_i$ by taking the 3-D spatial derivative of the spline at the channel locations, making use of a digital elevation model (DEM) if one is available.

The degree of the spline k is a design parameter (here set, but could also be optimised) that controls the smoothness of the cable path. For example, a linear spline ($k = 1$) produces a piecewise linear path with non-differentiable corners at knots, while a cubic spline ($k = 3$) produces a smooth path as shown in Fig. 1. The choice of spline degree therefore depends on the specific application, and further practical considerations may dictate the desired level of smoothness such as ensuring a level of ease and speed when laying out the cable according to the final design specification.

When deploying the optimized design in the field, the exact replication of channel locations is of course not feasible. This is, however, unlikely to cause a problem, since small deviations from the optimized layout will typically not lead to a significant performance degradation.

Another important aspect is the choice of channel spacing when designing a survey, which ideally should be the same as the desired channel spacing in the field. However, many design criteria have a computational cost that is quadratic or worse in the number of channels (e.g. in the number of ray-paths in ambient noise traveltime tomography $N_{\text{rays}} = N_{\text{cha}}(N_{\text{cha}} - 1)/2$, eigenvalue decomposition for dense matrices (G.H. Golub & C.F. Van Loan 2013), evaluation of Gaussian data likelihood with full covariance matrices (K.P. Murphy 2022) or are just intrinsically computationally expensive (e.g. Nested-Monte Carlo for Bayesian experimental design). There is therefore an incentive to use a larger channel spacing in the design process to reduce the computational cost of the optimization process. In some cases, the increase can be justified physically (e.g. traveltimes of seismic events recorded at channels close to each other

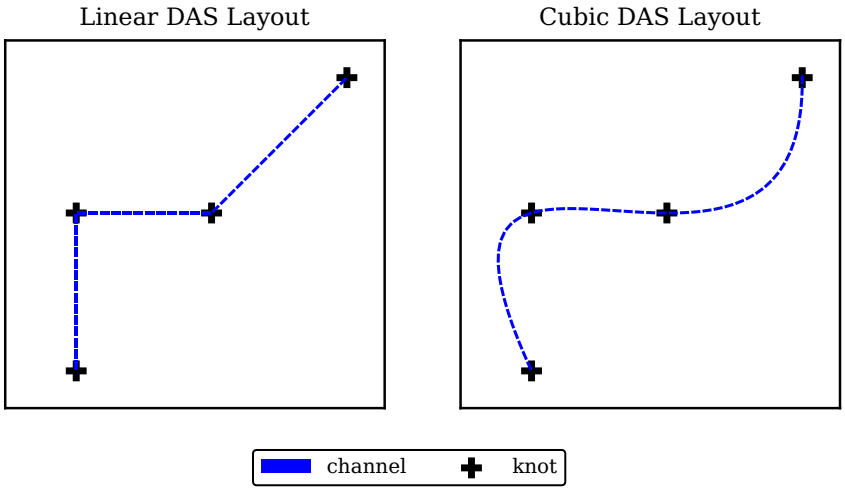

Figure 1. Example of a DAS cable parametrization with similar knots but different spline types: linear ($k = 1$) and cubic ($k = 3$).

provide little additional azimuthal and radial coverage, and often have correlated errors due to similar source–receiver raypaths). In other cases, it is purely a computational convenience to make the design process efficient, in which case care must be taken to ensure that the channel spacing is still sufficiently small for the chosen application. There is usually little incentive to choose an optimization channel spacing that is smaller than the gauge length, since successive channels will not then provide independent data (B.L.N. Kennett 2024).

2.2 Design criteria

Many different design goals might be considered when designing a DAS cable layout. In this study, we present computationally efficient design criteria, mostly from previous literature, that can be used to quantify common design goals. All these criteria share the characteristic that they use derived properties, such as phase picks or ambient noise correlations, instead of the full recordings of the seismic wavefield, simply because the data space (number of data points) required to describe seismic wavefields is enormous (e.g. H. Maurer *et al.* 2017; V. Krampe *et al.* 2021), which makes it extremely difficult to find optimal designs that are robust to nonlinearity in the physics relating wavefields to the parameters of interest (T. Guest & A. Curtis 2010). Nevertheless, the derived data space properties that we consider here cover a wide range of practical applications, while remaining sufficiently computationally efficient to allow for the global optimization of the cable layout.

2.2.1 Preliminaries on signal decay and sensitivity

Accounting for the signal strength of both seismic waves and laser signals along the cable is crucial when designing a DAS survey. To avoid the need for precise knowledge of noise levels and source magnitudes, we adopt a relative approach. We define a reference distance R_{ref} at which a signal arriving at a perfectly aligned cable (one oriented along the highest angular sensitivity) is assumed to have a signal-to-noise ratio (SNR) of one. The choice of reference distance should typically be such that it is not so high that all layouts perform equally well, but also not so low that all layouts perform poorly. Signal strengths just above the noise level are where the layout design has the most impact on performance, unless either of these cases are known to pertain to the real Earth.

Given this reference distance, three main factors determine the SNR: (1) the distance between the cable and a seismic source, (2) the distance along the cable from the interrogator and (3) the orientation of the incident seismic wavefield relative to the cable.

Without prior knowledge of seismic energy attenuation due to scattering or conversion to heat, we can assume that geometric spreading dominates the attenuation of energy (A.F. Baird *et al.* 2025). The seismic wavefield amplitude as a function of distance r from the source is then proportional to $1/r$ for spherically spreading body waves and $1/\sqrt{r}$ for cylindrically spreading surface waves (Fig. 2). While this provides a reasonable approximation, local magnitude scales enable more accurate modelling of the attenuation of seismic body wave phases. Although most magnitude scales are developed for traditional seismic sensors (L.K. Hutton & D.M. Boore 1987) and are not directly applicable to DAS, recent studies present empirical relationships between local magnitude and source distance for DAS (A.J. Barbour & B.W. Crowell 2017; A.J. Barbour *et al.* 2021; I. Lior *et al.* 2021, 2023; J. Yin *et al.* 2023; S. Baba *et al.* 2024). For P and S waves, we use the scale of J. Yin *et al.* (2023)

$$\log_{10}(A_i^{\text{P}}) = 0.437M - 1.269\log_{10}(R) + K_i^{\text{P}} \quad (1)$$

$$\log_{10}(A_i^{\text{S}}) = 0.690M - 1.588\log_{10}(R) + K_i^{\text{S}}, \quad (2)$$

where A_i^{P} and A_i^{S} are the peak amplitude of the DAS strain rate for channel i in microstrain/s (10^{-6}s^{-1}) for P and S waves respectively, M is the source magnitude, R is the hypocentral distance in kilometres and K_i^{P} and K_i^{S} are channel-specific factors that account for all local effects such as cable construction, installation, instrumental coupling and the variety of regional geology (see Fig. 2). The scale has been proven to be transferable between different settings after only minor calibration. If we use both P and S waves together, we need to ensure that they are scaled consistently. We do this by calculating a reference magnitude M_{ref} such that a P-wave at distance R_{ref} with perfect alignment to the

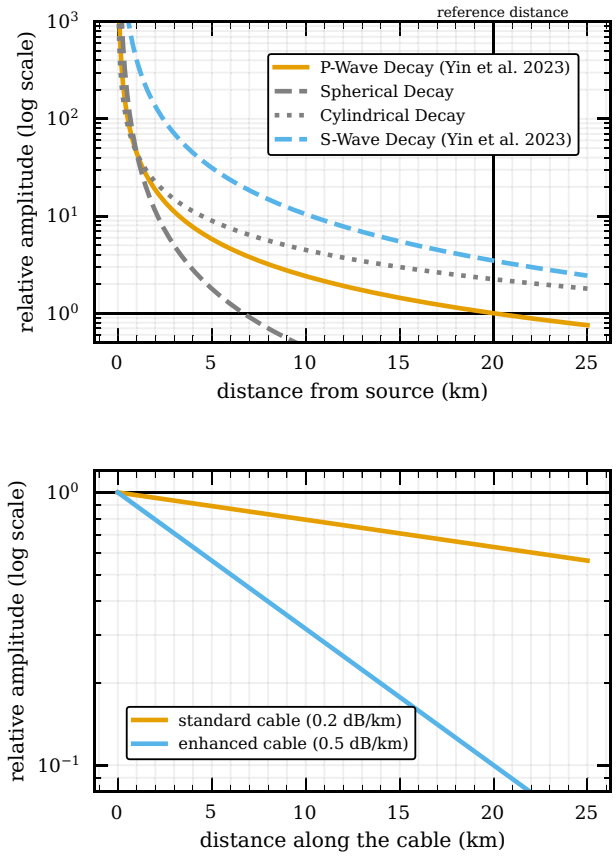

Figure 2. Top panel: Reduction in amplitude of seismic waves as a function of distance from source. Cylindrical decay of surface waves and spherical decay of body waves are shown alongside *P*- and *S*-wave decay derived from the local magnitude scale of J. Yin *et al.* (2023). Bottom panel: Attenuation of laser signal as a function of distance along the cable.

cable has an SNR of one, and then use this magnitude to calculate the *S*-wave amplitude at the same distance (this is done in Fig. 2, which results in the higher *S*-wave amplitude).

The laser signal propagating through the cable also experiences attenuation. For typical DAS cables, this attenuation is approximately $0.2\,\mathrm{dB\,km^{-1}}$ (P.S. Westbrook *et al.* 2020), resulting in a signal decay of $0.4\,\mathrm{dB\,km^{-1}}$, since the reflected signal must travel the distance twice (see Fig. 2). We assume a linear relationship between laser signal strength and SNR, consistent with the figures of Y. Miao *et al.* (2025). Enhanced scattering fibres can exhibit significantly higher attenuation values of $0.4 - 0.6\,\mathrm{dB\,km^{-1}}$ (P.S. Westbrook *et al.* 2020; A. Masoudi *et al.* 2021).

The primary distinction between single-component strain measurements along a DAS cable and traditional seismic sensor measurements lies in how cable orientation affects wavefield sensitivity, as well as in the measurement of strain rate rather than particle velocity. In our analysis of this angular sensitivity, we exclude wave amplitude factors and frequency or phase dependencies, as these characteristics are typically unknown for prospective arrivals prior to detection (T.S. Hudson *et al.* 2025).

The strain rate sensitivity ξ quantifies how the cable orientation affects the measured amplitude relative to the true seismic wave amplitude. It is defined as

$$A_{\mathrm{meas}} = \xi \cdot A_{\mathrm{wave}}, \tag{3}$$

where A_{meas} is the amplitude measured by the DAS cable and A_{wave} is the amplitude of the incident seismic wave. The sensitivity ξ ranges from 0 (no sensitivity) to 1 (maximum sensitivity) depending on the wave type and cable orientation. Constant multipliers in the following equations are removed since we use relative SNRs. For *P*, *SH* and *SV* waves, the sensitivity is given by (E.R. Martin *et al.* 2017; T.S. Hudson *et al.* 2025)

$$\xi_{\mathrm{P}} = \left|\cos^2(\theta)\sin^2(\varphi)\right| \tag{4}$$

$$\xi_{\mathrm{SH}} = \left|\cos^2(\theta)\sin(2\varphi)\right| \tag{5}$$

$$\xi_{\mathrm{SV}} = \left|\sin(2\theta)\cos(\varphi)\right|, \tag{6}$$

where θ represents the azimuth of the channel relative to the wave propagation direction on a plane in which the cable lies, and φ is the incidence angle, which is the angle of the plane wave relative to the plane-perpendicular angle (e.g. angle from vertical-down for a channel on a horizontal section of cable). Following T.S. Hudson *et al.* (2025), we define the *S*-wave sensitivity as

$$\xi_{\mathrm{S}} = \max\left(\sqrt{\frac{1}{2}\left(\xi_{\mathrm{SH}}^2 + \xi_{\mathrm{SV}}^2\right)}, \xi_{\mathrm{SV}}, \xi_{\mathrm{SH}}\right), \tag{7}$$

which allows us to combine the two *S*-wave polarization modes.

This anisotropic sensitivity creates complex patterns in the SNR as a function of azimuth and distance to the source. Fig. 3 illustrates the directional sensitivity and SNR for *P* waves across varying azimuths, distances and source depths for a horizontal cable. If the cable was dipping significantly, the sensitivity would become asymmetric. The SNR calculations assume a reference distance of $R_{\mathrm{ref}} = 10\,\mathrm{km}$ and use the local magnitude scale of J. Yin *et al.* (2023). The absence of sensitivity to broadside arrivals is evident, with the insensitive area below the channel widening as depth increases. The velocity model significantly affects body-wave phase sensitivity, as velocity that increases with depth generally results in smaller incidence angles and consequently reduced sensitivity.

Fig. 4 shows the equivalent analysis for *S* waves. Rather than a source with equal source magnitude, the same reference distance as for *P* waves is used to allow direct comparison. *S*-wave sensitivity is generally higher but exhibits a more complex pattern [dominated by the $\sin(2\theta)$ term for small incidence angles, and a combination of $\sin(2\theta)$ and $\cos^2(\theta)$ for larger ones]. The layered velocity model causes dramatic changes in sensitivity patterns whenever the first arrival changes to critically refracted waves which travel along a deeper interface. For a source at a depth of 0.5 km, this even creates a small region of zero sensitivity within the main lobe of the *S*-wave sensitivity pattern (see Fig. 4 panels for a source at 0.5 km depth). In practical applications, sensitivity and SNR patterns will deviate from the idealized patterns shown here and may be smoother due to heterogeneous velocity structures and phase conversions. Both factors could be accounted for by using more complex velocity models or smoothing the sensitivity and SNR patterns.

Similar to body waves, surface waves exhibit anisotropic sensitivity described by (E.R. Martin *et al.* 2017, 2021)

$$\xi_{\mathrm{rayleigh}} = \left|\cos^2(\theta)\right| \tag{8}$$

$$\xi_{\mathrm{love}} = \left|\sin(2\theta)\right|, \tag{9}$$

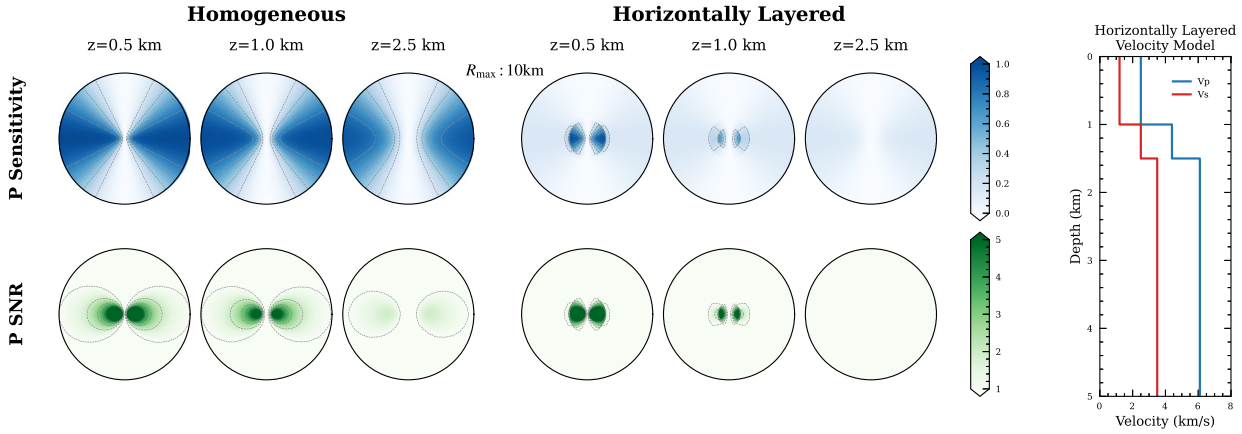

Figure 3. Sensitivity (top) and SNR (bottom) for *P* waves as a function of azimuth and distance to the source, for sources at different depths z in both homogeneous (left) and horizontally layered (right) velocity models. The SNR calculations assume a reference distance of $R_{\text{ref}} = 10$ km using the local magnitude scale of J. Yin *et al.* (2023). The radius of each circle is set to R_{ref}. The channel receiver is positioned at the centre and oriented along the east–west direction for a horizontal cable. To the right, the layered velocity model used is shown.

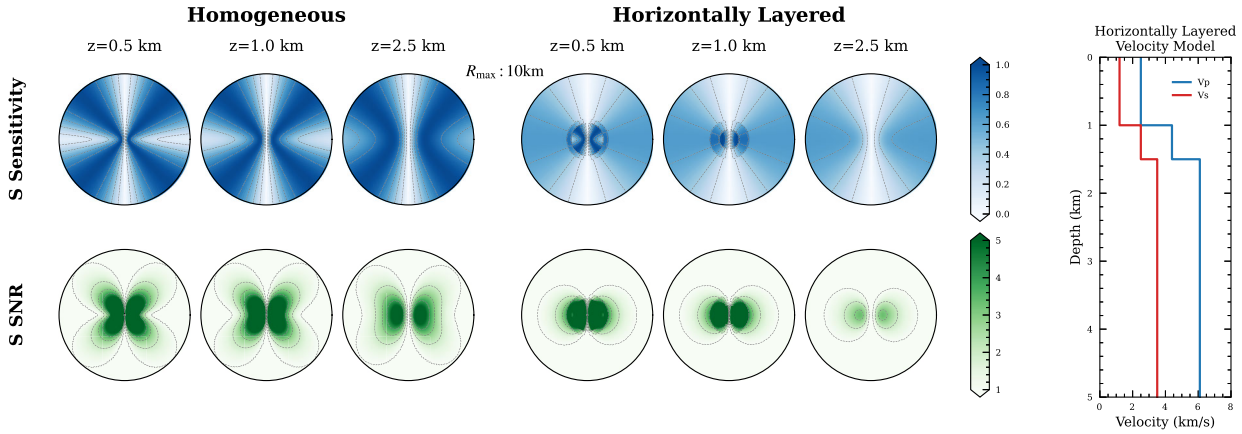

Figure 4. Sensitivity (top) and SNR (bottom) for *S* waves as a function of azimuth and distance to the source, for sources at different depths z in both homogeneous (left) and horizontally layered (right) velocity models. The SNR calculations assume a reference distance of $R_{\text{ref}} = 10$ km using the local magnitude scale of J. Yin *et al.* (2023). The radius of each circle is set to R_{ref}. The channel receiver is positioned at the centre and oriented along the east–west direction for a horizontal cable. To the right, the layered velocity model used is shown.

where θ is the azimuth of the channel relative to the wave propagation direction. Rayleigh wave sensitivity is therefore equivalent to *P*-wave sensitivity for a wave that propagates in the same plane as the cable, while Love wave sensitivity corresponds to *SV*-wave sensitivity for a wave that propagates in the same plane as the cable.

An interesting case arises for ambient noise analysis that involves cross-correlation between pairs of channels in the horizontal plane with azimuths θ_1 and θ_2, where ϕ represents the direction of the line that connects these channels. The ambient noise cross-correlation can be used to estimate the average group velocity between channels (A. Curtis *et al.* 2006) to perform ambient noise surface wave tomography (N.M. Shapiro *et al.* 2005; J. Fang *et al.* 2023), which requires no active source and can therefore be used to estimate the subsurface velocity structure passively. The approach is based on the assumption that the cross-correlation of ambient noise between two channels is proportional to the Green's function between these channels, at least for the wave phases or properties of interest (R. Snieder 2004; N.M. Shapiro *et al.* 2005).

The signal amplitude in the cross-correlation can be described by (E.R. Martin *et al.* 2021; J. Fang *et al.* 2023)

$$\xi_{\text{rayleigh-cc}} = \left|\cos^2(\theta_1 - \phi)\cos^2(\theta_2 - \phi)\right| \tag{10}$$

$$\xi_{\text{love-cc}} = \left|\sin 2(\theta_1 - \phi)\sin 2(\theta_2 - \phi)\right| \tag{11}$$

as illustrated in Fig. 5. For surface wave tomography that uses earthquake data, eqs (8) and (9) could be applied directly.

Several approximations were made in deriving the azimuthal dependencies: effects of wavelength, gauge length and local velocity structure were neglected. While beyond this study's scope, analytical expressions exist for some more complex cases (E.R. Martin *et al.* 2017, 2021), allowing straightforward incorporation of this information in cases for which it is available. The azimuthal dependencies of sensitivity and SNR presented here therefore represent first-order approximations that should be used with caution, but which nevertheless provide valuable insights for DAS cable layout design, as many of the incorporated effects are observed in field data (e.g. A. Mateeva *et al.* 2014; J. Yin *et al.* 2023; A.F. Baird *et al.* 2025).

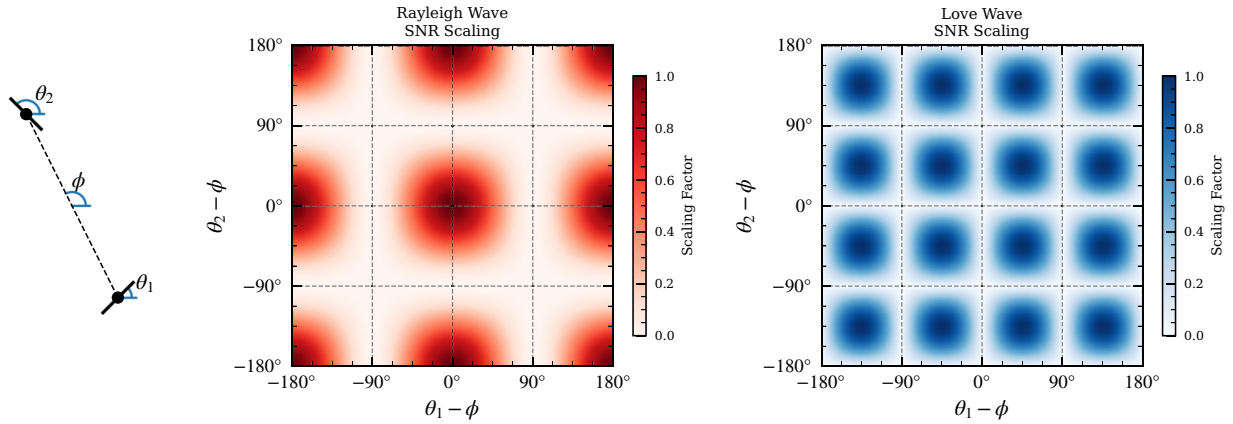

Figure 5. Sensitivity for Rayleigh (centre) and Love (right) waves as a function of the azimuths of the two channels relative to the wave propagation direction, which is set to have azimuth zero for the purposes of display. The sketch on the left illustrates the azimuths of the two channels θ_1 and θ_2 and the direction of the line connecting the two channels ϕ. Adapted from J. Fang *et al.* (2023).

2.2.2 Linearized traveltime tomography

Linearized traveltime tomography is a tool for imaging subsurface velocity structure using traveltime measurements between pairs of receivers or between sources and receivers. It relies on the assumption that ray paths can be approximated as fixed, allowing the inverse problem to be formulated as a linearized system of equations:

$$\mathbf{d} = \mathbf{A}\mathbf{m} + \boldsymbol{\epsilon}, \tag{12}$$

where $\mathbf{d}$ is the vector of observed data (interchannel time lags, or equivalently traveltimes), $\mathbf{m}$ is the model vector (group or phase velocity at a set of locations), $\mathbf{A} = \partial d_i / \partial m_j$ is the sensitivity matrix of partial derivatives of each datum d_i with respect to each model parameter m_j, and $\boldsymbol{\epsilon}$ is the noise vector. If the velocity model is parametrized on a grid of non-overlapping cells, $\mathbf{A}$ can be constructed from the ray paths between channels as $A_{ij} = l_{ij}$, where l_{ij} is the length of ray path i in cell j. Here, each ray defines the interchannel path followed by the wave packet for which traveltime data d_i were measured. While in our examples we follow the common approach of designing surveys using a homogeneous velocity model to calculate $\mathbf{A}$ (J. Fang *et al.* 2023), in general the best prior estimate of the velocity model in any particular survey area should be adopted.

The matrix $\mathbf{A}$ determines the sensitivity of the data to the underlying velocity model, and its eigenvalue spectrum can be used to quantify the inversion stability and information transfer from data to parameter estimates (W. Menke 2018). Since measurement errors propagate into the solution $\mathbf{m}$ parallel to each eigenvector of $\mathbf{L} = \mathbf{A}^T\mathbf{A}$ with an amplification of $1/\lambda_i$, where λ_i is the i-th eigenvalue of $\mathbf{L}$, optimal experimental design for linearized methods aims to maximize eigenvalues of $\mathbf{L}$. Fig. 6 illustrates how different cable layouts affect the eigenvalue spectrum for both Rayleigh and Love waves. For each design, we show the average sensitivity to each velocity grid cell across all data, and demonstrate the effect on inversion results with a checkerboard model. Data for the checkerboard inversion were generated with a seismic ray tracer (B. Giroux 2021), which accurately models the ray paths in the heterogeneous checkerboard model, and were inverted using the sensitivity matrix based on a homogeneous prior model. Layouts with high eigenvalue spectra exhibit both better sensitivity coverage and improved resolution of the checkerboard model.

Several approaches exist for quantifying eigenvalue positivity in optimal experimental design (A.C. Atkinson & A.N. Donev 1992; A. Curtis 2004b). A-optimality (A. Curtis & R. Snieder 1997; V. Krampe *et al.* 2021), D-optimality (G.E.P. Box & H.L. Lucas 1959; A. Kijko 1977a, b; N. Rabinowitz & D.M. Steinberg 1990; D.M. Steinberg *et al.* 1995; A. Curtis 1999a, b), and the relative eigenvalue range (RER) (H. Maurer *et al.* 2009) are the most commonly used criteria in geophysical applications.

In the examples in this study, we use the D-optimality criterion Σ_D, which is defined as

$$\Sigma_D = |\det(\mathbf{L})| = \prod_{i=1}^{N} \lambda_i = \sum_{i=1}^{N} \log(\lambda_i) \tag{13}$$

and relates directly to the volume of the posterior covariance matrix (G.E.P. Box & H.L. Lucas 1959). To allow the criterion to be applied to underdetermined problems, a threshold λ_{thr} is often applied (A. Curtis 1999a), below which eigenvalues are set to a penalty term λ_{pen}. The penalty term should be a sufficiently large negative number to ensure that almost all possible logarithm of eigenvalues exceed λ_{thr}. The D-optimality criterion in eq. (13) measures the volume under the logarithmic eigenvalue spectrum, but for ease of interpretation, in mixed or underdetermined problems, we define an adapted normalized D-optimality criterion Σ_D^* as

$$\Sigma_D^* = 1 - \frac{\sum_{i:\lambda_i \geq \lambda_{\text{thr}}} \log\left(\frac{\lambda_i}{\lambda_{\max}}\right) + N_{\text{below}} \cdot \lambda_{\text{pen}}}{N \cdot \lambda_{\text{pen}}}, \tag{14}$$

where $\lambda_{\max}$ is the maximum eigenvalue, and N_{below} is the number of eigenvalues below the threshold. This measure is bounded between 0 and 1, with 1 indicating a perfect design where all eigenvalues are equal to $\lambda_{\max}$, and 0 indicating a design where all eigenvalues are below the threshold λ_{thr}. Importantly, this represents only a different formulation of the (normalized) D-optimality criterion and does not change the optimal design.

The threshold and penalty term are necessary due to the ill-conditioning of the sensitivity matrix $\mathbf{L}$ (A. Curtis 1999a). If the sensitivity matrix is regularized by introducing prior knowledge in the form of an *a priori* model covariance matrix $\mathbf{C}_m$ and a

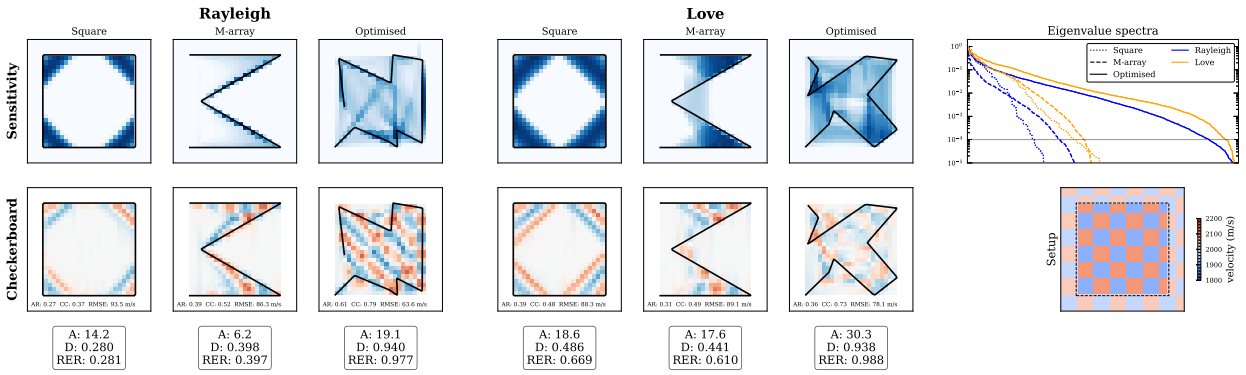

Figure 6. Schematic illustration of how different cable layouts (all of the same length) affect various measures of information about the model provided by recorded Rayleigh (left) and Love (right) wave data. The top row shows the average over all data of the sensitivity to each velocity grid cell for a checkerboard model; the bottom row shows the results of inverting a checkerboard model using the sensitivity matrix $\mathbf{A}$ for each layout. The side length of the plots is 3000 m and the reference distance used for the attenuation of seismic energy is 7500 m for Rayleigh waves and 2500 m for Love waves, which are chosen in a way that the different layouts produce a range of eigenvalue spectra. The normalized eigenvalue spectrum is shown top right, and the true velocity model is shown bottom right with the square array overlain for reference. Normalized A-optimality Σ_A^*, D-optimality Σ_D^* ($\lambda_{\text{thr}} = 10^{-10}$), and relative eigenvalue range (RER) Σ_{RER} ($\lambda_{\text{thr}} = 10^{-5}$) values are provided below each layout labelled A, D and RER, respectively. The optimized layouts are D-optimal. At the bottom of each checkerboard result, common resolution metrics are provided: (AR): amplitude recovery (higher is better), (CC): correlation coefficient (higher is better) and (RMSE): root mean square error (lower is better).

data covariance matrix $\mathbf{C}_d$ (H. Maurer *et al.* 2010), the original D-optimality criterion can be used without the need for a penalty term. While including such information lies beyond the scope of this design methodology study (since it involves case-dependent prior information) it is important to note that such prior information can make the optimization process more robust and allows it to focus better on the least constrained parts of the model according to the prior information.

The A-optimality criterion is computationally more efficient as it does not require the full eigenvalue spectrum to be calculated: the sum of eigenvalues is equal to the trace of $\mathbf{L}$, and the largest eigenvalue (used for normalization) can be estimated using the power method (A. Curtis & R. Snieder 1997; A. Curtis 1999a, b). This efficiency comes at the cost of often leading to designs with a small number of large eigenvalues at the expense of many small eigenvalues. For an example of this, see the Rayleigh wave results in Fig. 6, where the square design performs reasonably well according to the A-optimality criterion, but the checkerboard model is poorly resolved, which is in line with the findings of V. Krampe *et al.* (2021) in the context of full waveform inversion. In this study, the scenarios considered are small enough to calculate the full eigenvalue spectrum and therefore employ the adapted D-optimality criterion Σ_D^* as our design criterion. For a detailed discussion of linearized optimal experimental design for seismic tomography, we refer to A. Curtis (2004b).

We include attenuation effects and anisotropic sensitivity by first calculating all ray paths between all pairs of channels, and then removing those for which the SNR is below a threshold value. The SNR depends on the interchannel distance and alignment and is set to one for channels with perfect alignment at a distance of R_{ref}.

In recent decades, several improvements to linearized experimental design have been proposed. These advances account for prior knowledge in a Bayesian, yet still linearized, manner (e.g. Q. Long *et al.* 2015; A. Alexanderian 2021; Y. Englezou *et al.* 2022), and enhance computational efficiency for large-scale problems (e.g. K. Wu *et al.* 2023a, b, c; A. Mercier *et al.* 2025), or aim to increase robustness against model uncertainty (A. Alexanderian *et al.* 2024) and worst-case scenarios (A. Chowdhary *et al.* 2024). Since this study focuses on DAS cable layout optimization and the computational cost is relatively low for the scenarios considered here, we do not apply these methods, but they can be directly integrated into our optimization process when the required prior information is available. There are also important assumptions in linearized ambient noise tomography that could be relaxed if appropriate prior information is available. A heterogeneous distribution of ambient noise sources, for example, would change the accuracy of interferometric empirical Green's function estimates, and hence traveltimes, as a function of interreceiver path azimuth (L. Li *et al.* 2020). This could be accounted for, in part, by adjusting the expected SNR of each ray-path accordingly.

2.2.3 *Probabilistic source location*

Linearized experimental design, as introduced in the previous section, efficiently optimizes experimental designs but is inherently limited by its reliance on linearization and cannot account for the full nonlinearity in the physics of the problem (A. Curtis 2004a; D. Strutz & A. Curtis 2024). As an example of fully nonlinear Bayesian experimental design, we consider the optimization of a DAS layout for probabilistic source location. In this approach, we aim to estimate the posterior probability distribution of the source location $\mathbf{m}$ given the observed data $\mathbf{d}$ and design $\boldsymbol{\xi}$

$$p(\mathbf{m} \mid \mathbf{d}, \boldsymbol{\xi}) = \frac{p(\mathbf{d} \mid \mathbf{m}, \boldsymbol{\xi})\, p(\mathbf{m})}{p(\mathbf{d} \mid \boldsymbol{\xi})}, \tag{15}$$

where $p(\mathbf{d} \mid \mathbf{m}, \boldsymbol{\xi})$ is the data likelihood given the source location and design, and $p(\mathbf{m})$ is the prior distribution of the source location. The prior distribution describes our belief about where seismicity is most likely to occur in the subsurface before any data observation from the proposed survey, while the likelihood quantifies the probability of observing the recorded data given the model parameters and experimental design.

The data likelihood function should take the form of expected observational uncertainties, so we define it as a multivariate

Gaussian distribution

$$p(\mathbf{d} \mid \mathbf{m}, \boldsymbol{\xi}) = \mathcal{N}(\mathrm{F}(\mathbf{m}, \boldsymbol{\xi}), \boldsymbol{\Sigma}_d), \tag{16}$$

where $\mathrm{F}(\mathbf{m}, \boldsymbol{\xi})$ is the forward function that predicts arrival times for a given source location and design, and $\boldsymbol{\Sigma}_d$ is the expected data covariance matrix. The forward function typically involves ray tracing to calculate expected arrival times of seismic phases at channels based on the source location and velocity model.

The data covariance matrix incorporates the effects of signal decay and sensitivity discussed earlier, and can be modelled as:

$$\boldsymbol{\Sigma} = \boldsymbol{\Sigma}_{\text{pick}} + \boldsymbol{\Sigma}_{\text{vel}} + \boldsymbol{\Sigma}_{\text{obs}}, \tag{17}$$

where $\boldsymbol{\Sigma}_{\text{pick}}$ represents the uncertainty in phase picking, $\boldsymbol{\Sigma}_{\text{vel}}$ accounts for uncertainty in the velocity model and $\boldsymbol{\Sigma}_{\text{obs}}$ quantifies general observation noise such as channel location uncertainty or other measurement errors (D. Strutz & A. Curtis 2025b). The first two terms are functions of the source location $\mathbf{m}$ and the design $\boldsymbol{\xi}$, while the third term is typically a constant value.

We convert the SNR into picking uncertainty $\boldsymbol{\Sigma}_{\text{pick}}$ via an information-theoretic approach (K. Aki 1976; A. Fuggi *et al.* 2024):

$$\left(\Sigma_{\text{pick}}\right)_{ii} = \left[\log_2\left(1 + \frac{20\log_{10}\mathrm{SNR}(\mathbf{m}, \boldsymbol{\xi})_i}{K}\right) 2\, f_{\max}\right]^{-2}, \tag{18}$$

where $\mathrm{SNR}(\mathbf{m}, \boldsymbol{\xi}) = A_{\text{signal}}(\mathbf{m}, \boldsymbol{\xi}) / A_{\text{noise}}(\boldsymbol{\xi})$ is the signal-to-noise ratio of the signal amplitude $A_{\text{signal}}(\mathbf{m}, \boldsymbol{\xi})$ and the noise amplitude $A_{\text{noise}}(\boldsymbol{\xi})$, and $f_{\max}$ is the maximum frequency of the recorded signal. The absolute value of $A_{\text{noise}}(\boldsymbol{\xi})$ need not be known since the reference distance R_{ref} normalizes the SNR. Relative changes in $A_{\text{noise}}(\boldsymbol{\xi})$, for example due to local conditions or noise sources, can be included by multiplying the SNR of a given channel by a factor that accounts for the change in noise level. The empirical factor $K = 10$ in eq. (18) is chosen to align with empirical estimates of picking uncertainty from C.A. Zelt & D.A. Forsyth (1994) and J. Pablo Canales *et al.* (2000), and differs from the value used by A. Fuggi *et al.* (2024) and K. Aki (1976). The exact values of both K and the maximum frequency $f_{\max}$ are not critical for design optimization, as they scale the picking uncertainty uniformly across all channels while preserving the key characteristic of rapidly increasing uncertainty at low SNR values.

For the velocity model uncertainty, we assume that the variance of the traveltime errors is proportional to the traveltime itself:

$$\left(\Sigma_{\text{vel}}\right)_{ii} = d_i \cdot \varsigma_{\text{vel}}^2, \tag{19}$$

where d_i is the traveltime of the i-th phase arrival and ς_{vel} is a scaling factor that determines the magnitude of uncertainty we assume in the seismic velocity model. This assumption is based on a Gaussian random walk model, where the variance of the distance from a reference point (in our case, the mean arrival time) is proportional to the time (here arrival time). Intuitively, this means that the longer the traveltime, the more uncertainty it accumulates along its path.

While incorporating velocity model knowledge into the forward model is straightforward (albeit potentially computationally expensive), quantifying arrival time uncertainty is more complex. The approach presented here is one of many possible methods, with the optimal choice depending on the specific application and available prior information. Alternative approaches in the literature include using a linear relationship between arrival time and its standard deviation (A. Tarantola & B. Valette 1982; A. Fuggi *et al.* 2024), polynomial fits that describe uncertainty as a function of source–receiver distance and depth (J. Callahan *et al.* 2025), or (heuristic) estimates based on the attenuation of seismic energy (A. Curtis *et al.* 2004).

In eq. (19), we have assumed that the measurement uncertainties at different receivers are independent of each other. This is not the case if the seismic wave paths to nearby receivers travel similar routes through the subsurface, therefore accumulating similar deviations. While exactly quantifying this dependence is difficult, we use a heuristic approach (A. Tarantola & B. Valette 1982; J. Callahan *et al.* 2025) and base the correlation of the uncertainties on the interreceiver distances l_{ij} defined as:

$$C_{ij} = \exp\left(-\frac{1}{2}\frac{l_{ij}^2}{l_{\text{cor}}^2}\right), \tag{20}$$

where l_{cor} is the correlation length. If correlations are expected, the covariance matrix becomes:

$$\hat{\boldsymbol{\Sigma}}_{\text{vel}} = \boldsymbol{\Sigma}_{\text{vel}}(\mathbf{m}, \boldsymbol{\xi}) \cdot \mathbf{C}. \tag{21}$$

Exactly how to choose K, $f_{\max}$, ς_{vel} and l_{cor} depends on the specific application and available prior information. As mentioned earlier, the absolute values of K and $f_{\max}$ are less critical since they scale the picking uncertainty uniformly across all channels. While $f_{\max}$ can be estimated from prior knowledge of the expected frequency content of seismic signals in the area of interest, K describes the efficiency of information extraction from a seismic signal in general and should therefore not vary significantly between applications. For more information on how to choose these parameters, we refer to D. Strutz & A. Curtis (2025b), which also contains an example of how to estimate ς_{vel} from a set of velocity models. Note that ς_{vel} can significantly affect the design optimization results. If unsure about how to choose ς_{vel} and l_{cor}, or which functional dependence of velocity model uncertainty to use, we recommend performing traveltime calculations for a range of prior velocity models and estimating the arrival time uncertainties and their correlations from the resulting traveltime variations.

As a design criterion for probabilistic source location, we use the expected information gain (EIG) (D.V. Lindley 1956):

$$\mathrm{EIG} = \mathbb{E}_{p(\mathbf{d}|\boldsymbol{\xi})}\Big\{\mathrm{I}[p(\mathbf{m} \mid \mathbf{d}, \boldsymbol{\xi})] - \mathrm{I}[p(\mathbf{m})]\Big\} \tag{22}$$

$$= \mathbb{E}_{p(\mathbf{m})}\Big\{\mathrm{I}[p(\mathbf{d} \mid \mathbf{m}, \boldsymbol{\xi})] - \mathrm{I}[p(\mathbf{d}|\,\boldsymbol{\xi})]\Big\}, \tag{23}$$

where $\mathrm{I}[p]$ denotes the Shannon information (C.E. Shannon 1948; T.M. Cover & J.A. Thomas 2006) of distribution p. The EIG quantifies the expected reduction in uncertainty about the source location after we observe the data, compared to its prior uncertainty. We calculate the EIG via the robust nested Monte Carlo (NMC) method (K.J. Ryan 2003; X. Huan & Y.M. Marzouk 2013) to avoid assumptions about the posterior distribution. For detailed treatment of the EIG in geophysical applications, see D. Strutz & A. Curtis (2024).

2.2.4 Other design criteria

The design optimization process can be adapted to any design criterion that takes a cable layout as input and returns a scalar value as output. An example of another criterion is the offset-azimuth distribution for constraining azimuthal anisotropy (A.

Fichtner & C. Hofstede 2022). The EIG used for the source location criterion could be adapted to probabilistic moment tensor estimation. This would require more prior information, such as phase amplitude models and uncertainty, and would come at a higher computational cost since more samples would be necessary to estimate the EIG. Another possible extension is to apply the earlier work of D. Strutz & A. Curtis (2025a) to DAS cables and treat them as a single array (S.P. Näsholm *et al.* 2022) or multiple sub-arrays (S. Ben-Zeev & I. Lior 2025) for seismic source location. The only additional requirement for this would be to define uncertainty estimates for the backazimuth and slowness estimates based on the SNR of the recorded signals and the array response function (J. Schweitzer *et al.* 2012).

2.3 Design optimization

The optimization of DAS cable layouts is a nonlinear optimization problem for which ideally we want to find the global optimum. Since gradient-based optimization methods would require the design criterion to be differentiable with respect to the knots describing the cable layout, and are often prone to local optima, we choose to use derivative-free optimization methods, specifically evolutionary algorithms (P.A. Vikhar 2016) due to their flexibility and robustness. These algorithms work by evolving a population of layouts of size N_{pop} over a number of generations. In each generation, the population is evaluated using the design criteria and the best layouts are selected and used to form the next generation. During the optimization process, the population is mutated (partially altered) and recombined (e.g. components of pairs of designs are exchanged) to explore the design space (see Figs 7a and b for an illustration of these operations) and move towards the optimal solution. While they are not guaranteed to find the global optimum in finite time, they work well in practice for many problems and can escape local optima.

To optimize the cable layout, we optimize the knot locations $\mathbf{k}_i$, from which channel locations are interpolated using a given channel spacing and spline degree k (which could also be optimized). All knots and channels must lie within a bounded area and cannot be positioned within pre-defined restricted areas, while the cable layouts must not exceed the maximum permissible cable length. Additionally, user-defined fixed knots between the optimizable knots can constrain the cable to pass through certain locations or follow a specific path for a portion of the cable.

An important aspect of evolutionary algorithms is the generation of the initial population. If the initial population is too similar, the optimization process may become stuck in local optima and fail to explore the design space effectively. Conversely, if the initial population is generated completely randomly, nearly all layouts may violate design constraints such as maximum cable length and restricted areas. This is particularly problematic when design constraints are strict, making the generation of valid layouts computationally expensive.

To address this challenge, we use one or more proposal cable layouts to guide the generation of the initial population. Proposal layouts are splines with N_{prop} manually defined knots that represent reasonable starting points for the optimization process. These layouts provide a convenient means of introducing expert knowledge and heuristics, leading to faster convergence while balancing the risk of biasing results towards the proposals.

The initial population generation process proceeds as follows (illustrated in Fig. 7d). We begin with a set of proposal layouts, which need not be of the same length, and assign a normalized weight w_{prop} to each proposal. The weight controls the fraction of the initial population generated from each proposal and is typically set to $w_{\text{prop}} = 1/N_{\text{total}}$, where N_{total} is the total number of proposal layouts. For each proposal layout, we create $N_{\text{pop}} \times w_{\text{prop}}$ initial layouts, where N_{pop} is the total population size.

To generate a single initial cable layout, we employ a two-stage perturbation process. First, we perturb the proposal knots using a Gaussian distribution with standard deviation ϵ_{prop}. Secondly, we randomly sample N_{knots} knot points along a spline that interpolates the perturbed proposal knots, ensuring that all layouts in the initial population have the same number of knots. These sampled knots are then further perturbed using another Gaussian distribution with standard deviation ϵ_{knot}.

This two-stage approach is important for constraint satisfaction. If perturbations were applied only to the final knot locations, the resulting cable layout could easily violate the maximum cable length constraint. The separation of proposal perturbation from knot location perturbation helps maintain feasible layouts. For layouts with many knots, perturbations can be correlated with the distance along the cable between knot points, which further helps prevent violations of the permissible cable length.

If the resulting cable layout violates any constraints, such as exceeding the maximum cable length or entering restricted areas, it is rejected and a new one is generated. This process repeats until a sufficient number of valid layouts have been created for each proposal. When design constraints are strict, only a small fraction of possible knot locations will result in permissible cable layouts. Therefore, proposal points and perturbation strengths must be chosen carefully to ensure the initial population can be generated within a computationally tractable number of iterations.

This approach balances manual input with automated generation, enabling the incorporation of expert knowledge while effectively exploring the design space. Although the method described above works well for the examples in this study, it represents one of many possible approaches for generating initial populations, ranging from completely random layouts to fully hand-crafted designs.

Once the initial process is complete, the population is evolved over several generations. Various strategies can be employed to evolve the population (e.g. R. Storn & K. Price 1997; A.G. Gad 2022), and we chose to use a genetic algorithm (GA) (J.H. Holland 1984, 2021) as it performed best in our tests. The genetic algorithm evolves the population by selecting the N_{select} best layouts, applying simulated binary crossover (K. Deb *et al.* 2000) to combine them in random ways, introducing random mutations via polynomial mutation and retaining the best N_{pop} layouts for the next generation. This process iterates until the maximum number of generations or another stopping criterion is reached. Early termination is often beneficial when the population shows no improvement over several generations, thus balancing solution quality with computational efficiency.

Sorting layouts by their design criterion is straightforward for single-objective optimization. For multi-objective optimization, we use the non-dominated sorting genetic algorithm (NSGA-II) (K. Deb *et al.* 2000). This algorithm sorts the population into non-dominated (Pareto) fronts and selects the best layouts

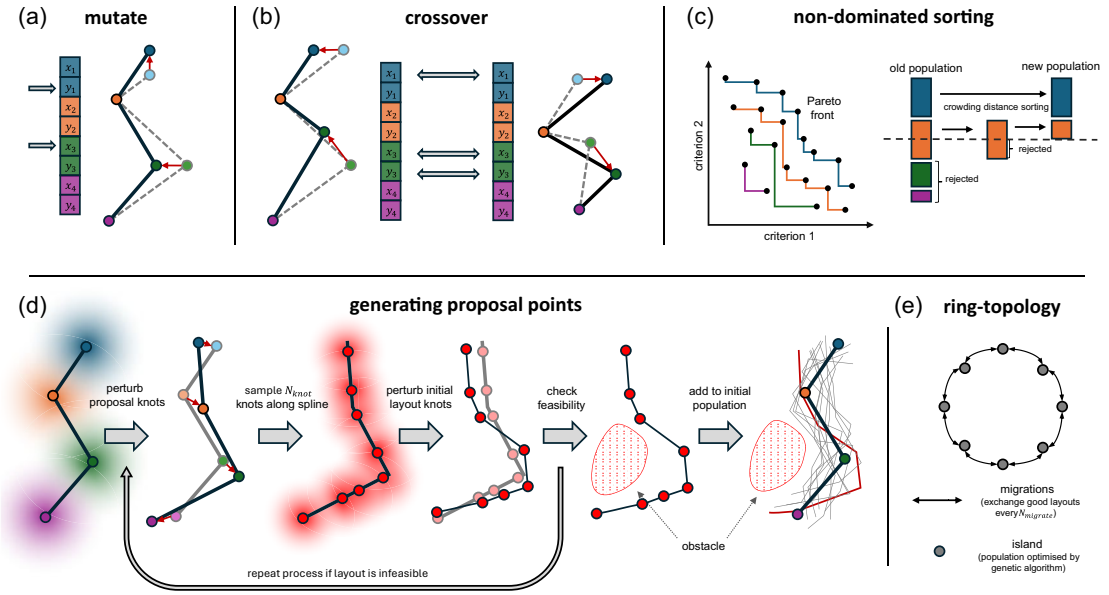

Figure 7. Schematic illustration of selected steps in the design optimization process for DAS cable layouts. (a) and (b) respectively illustrate the mutation and crossover operations used to evolve the population of candidate layouts. (c) shows a schematic example of how the non-dominated sorting algorithm works, where the layouts (black dots) are first sorted into non-dominated fronts (coloured lines) from which the best layouts are selected for the next generation. If a front exceeds the population size threshold, layouts from this front are selected based on crowding distance sorting, which ensures layouts are well distributed along the front. (d) generation of the initial population from a single proposal layout. For more details, see the text. (e) illustrates how layouts in a ring topology are exchanged between islands.

from each front, using a crowding distance to ensure diversity when necessary (see Fig. 7e for an illustration). The Pareto front is the set of layouts that cannot be improved in any of the objectives without degrading at least one of the other objectives. It is constructed by identifying all layouts in the population that are not dominated by any other layouts - meaning no other solution is better in all objectives while being strictly better in at least one. The crowding distance measures how close the layouts are to each other in the design criterion space. The final Pareto front allows one to choose the best layout for each design criterion individually, or a compromise between them.

Since the design optimization process is non-deterministic, results will vary between runs unless the random seed is fixed. To ensure robust results, we recommend running the optimization multiple times using different seeds. We achieve this efficiently by employing the generalised island model (D. Izzo *et al.* 2012), in which each island (a population and an evolution strategy) evolves independently, except that periodically (every N_{migrate}) it exchanges layouts with other islands in a conceptual archipelago. This exchange of information improves the convergence of the optimization process while allowing for parallelization with minimal communication overhead (D. Izzo *et al.* 2012). In this study, we use a ring topology, where each island exchanges layouts only with its two neighbours (see Fig. 7e for an illustration). The minimal communication overhead allows the optimization process to scale efficiently with the number of available CPU cores, with near-linear scaling when each island is assigned to a separate core. Further parallelization is possible at two additional levels: (1) evaluating multiple layouts within each island simultaneously, and (2) parallelizing the computation of design criteria themselves. Neither approach was implemented in this study, but the former should also achieve near-linear scaling, though with higher communication overhead than the island-level parallelization.

We use the pagmo library (F. Biscani & D. Izzo 2020) to implement both the evolutionary algorithms and the generalized island model. If sufficient computational resources are available, islands can be set up with different evolutionary strategies to further increase the robustness of the results.

3 SLOPE INSTABILITY CASE STUDY

To demonstrate the design optimization process, we use the Cuolm da Vi slope instability project (T. Kiers *et al.* 2026b) in Central Switzerland, one of the largest slow-moving slope instabilities in the Alps, as a case study. The instability spans an area of approximately 1.5 km^2, with an elevation difference of around 800 m (see Fig. 8). Its topography and the presence of inaccessible areas provide a challenging real-world scenario for the design optimization process. The instability is currently monitored, among other methods, by a 6.5 km long DAS cable deployed in the shoulder region of the slope (T. Kiers *et al.* 2026b). Here, we assess whether alternative layouts could provide additional information for either seismic source location or tomography.

3.1 Design constraints and initial layouts

The viable area (the area in which the cable can be deployed) is defined by the concave hull around the locations of over 1000 autonomous nodes deployed in early summer 2022, which covered most of the shoulder and slope of the instability (see Fig. 8). Topographic data was provided by the Swiss Federal Office of Topography (swisstopo).

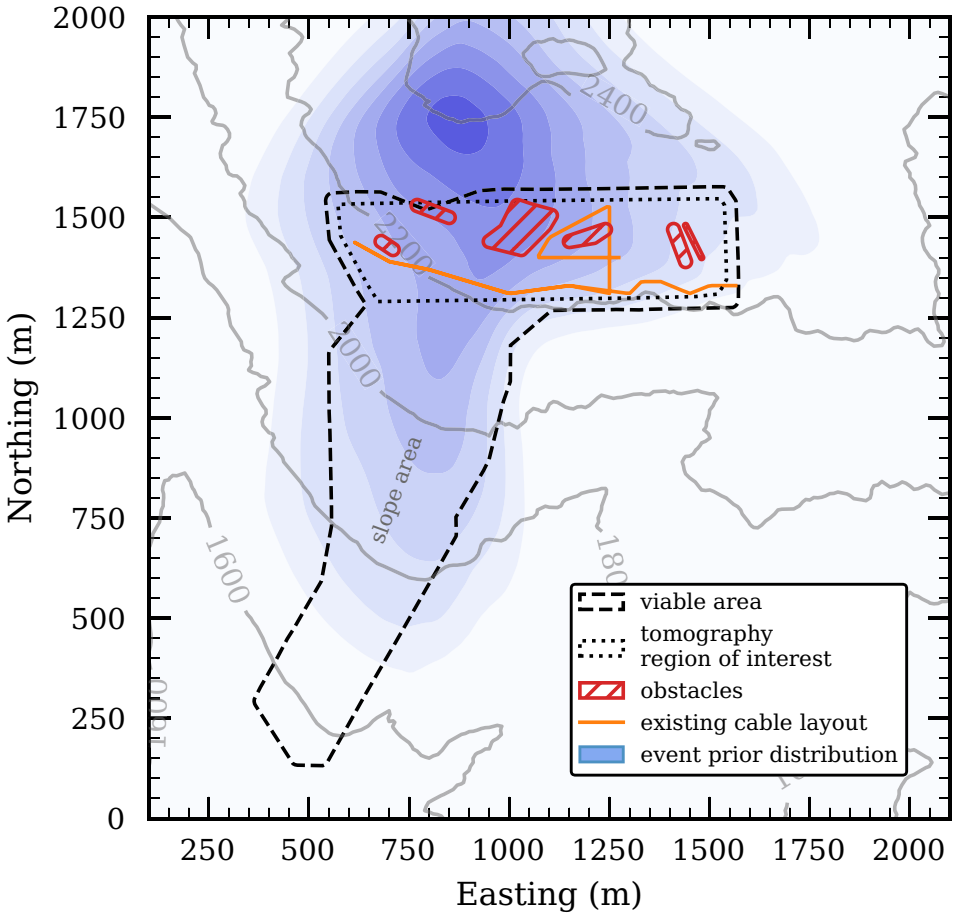

Figure 8. Cuolm da Vi slope instability in Central Switzerland, showing the viable area (dashed black), the shoulder area (dotted black), the obstacles (red), the existing DAS cable (orange) and the event prior distribution (blue contours, darker blue is more probable). The topography is shown in grey contour lines. The coordinates are local Cartesian coordinates.

For the *P*-wave source location scenario, we set the maximum cable length to 1700 m, which matches the length of the existing cable when excluding doubled-back segments and portions outside the viable area (see Fig. 8). This constraint allows for direct comparison with the current deployment. For the Rayleigh wave tomography and multi-objective optimization scenarios, we increase the maximum cable length to 2500 m. This extended length corresponds to the total cable length when doubled-back segments are included, providing sufficient coverage of the shoulder area to effectively perform tomography. Since the cable was not deployed with the tomography scenario in mind, a fair comparison is only possible for the source location scenario.

Unless otherwise stated, the cable takes the form of a linear (k =1) spline with 10 knots. A fixed point at (1610 m, 1330 m) ensures that the cable starts at the point where the existing cable enters the shoulder region (see Fig. 9). The channel spacing is set to 10 m, which is the same as the gauge length of the existing cable for the Rayleigh wave tomography scenario, but to 100 m for the *P*-wave source location scenario to reduce the computational cost of the optimization process (see Section 3.2 for the justification of this choice). Within the viable area, we define several restricted areas where the cable cannot be deployed. These correspond to crevasses, boulders or rock outcrops where ground coupling is difficult to achieve, and other areas where the cable cannot be deployed (red areas in Fig. 8).

The initial population is generated from manually selected proposal layouts (using an interactive plot of the study area) that cover the area of interest in a variety of distinct ways, each chosen based on heuristics and informed by expert knowledge. An intentional focus during the manual selection is placed on proposals that weave through the obstacles to ensure these paths are well represented in the initial population, as they are otherwise difficult to find during the optimization process. If there were significantly more of these narrow paths, the generation of the initial population would need to be adapted, for example by using a unique perturbation for each proposal knot (e.g. keeping part of the proposal layout fixed, while perturbing other knots more strongly), providing a large number of proposals by hand or changing to a different method to generate the initial population (e.g. graph-based methods, which could model the network of viable paths through the obstacles). The initial population is generated from the proposal layouts, as described in Section 2.3. Perturbations of $\epsilon_{\text{prop}} = 50$ m and $\epsilon_{\text{knot}} = 25$ m are used, along with a correlation length along the cable of 100 m. An example of a proposal layout and the derived initial population is shown in Fig. 9. The example shown is specific to the *P*-wave source location scenario. The proposals and therefore the initial population for the other scenarios differ slightly to account for the different design criteria and cable lengths.

For the optimization process, we use a population size of $N_{\text{pop}} = 128$ for single-objective optimization and $N_{\text{pop}} = 1028$

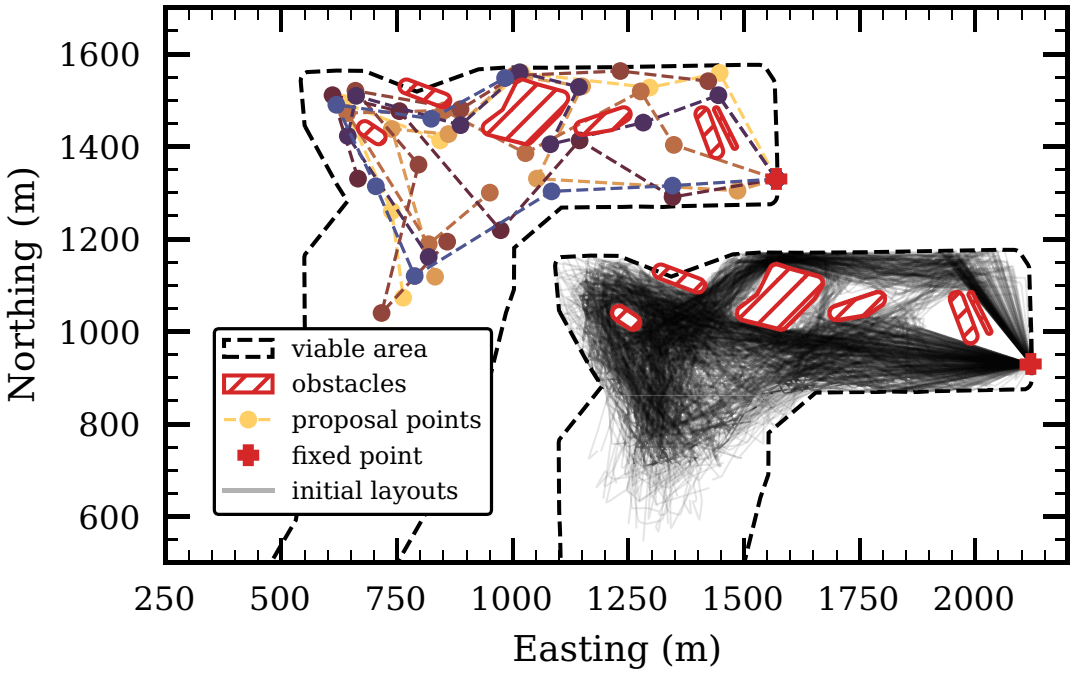

Figure 9. Proposal layouts and initial population for the Cuolm da Vi case study. The scale is the same as in Fig. 8. The initial population has been shifted down and to the right compared to the proposal layouts for better visibility. Only a subset of 500 initial layouts is shown.

for multi-objective optimization for each of the 16 islands in the archipelago. The population size for multi-objective optimization is substantially larger to ensure sufficient diversity all along the Pareto front. The population is evolved for 1000 generations with migrations occurring every 20 generations. Appendix A provides benchmarks on the trade-offs between population size, migration step-size, number of knots and spline degree.

3.2 *P*-wave source location

First, we optimize the cable layout for *P*-wave source location, using the EIG as the design criterion. In addition to the design constraints above, we must define the prior distribution and the data likelihood. We assume that the event prior distribution follows the surface displacement pattern (F. Amann 2006), with most potential events occurring just north of the shoulder region (see Fig. 8). The horizontal components of the prior distribution are described by a normalizing flow (E.G. Tabak & C.V. Turner 2013; L. Dinh *et al.* 2014) which is fitted to the surface displacement, while the vertical component is assumed to be distributed uniformly between depths of 0 and 300 m.

Although detailed velocity models are available for parts of the instability due to an exceptionally dense monitoring campaign (T. Kiers *et al.* 2026a), we use a homogeneous velocity model with a *P*-wave velocity of $V_\mathrm{P} = 1500\ \mathrm{m\,s^{-1}}$ to better represent typical real-world scenarios where detailed subsurface information is limited. To account for a shallow low-velocity layer, we limit the maximum incidence angle to 30°, which approximates the effect that most first arrivals will be refracted and therefore have a small incidence angle. The arrival uncertainty is determined by the picking uncertainty term ($R_\mathrm{ref} = 1000$ m), the velocity uncertainty term ($\varsigma_\mathrm{vel} = 0.05$) and the general observational uncertainty ($(\Sigma_\mathrm{obs})_{ii} = 0.01$ s) (F. Walter *et al.* 2020). To avoid data correlations due to similar ray paths for nearby channels and for computational efficiency, we downsample the channel spacing by a factor of 10 to 100 m (we take the central channel).

The number of samples used for the NMC estimate of the EIG is set to $N = 1000$, which provides a good balance between accuracy and computational cost. Although the absolute EIG value changes markedly with increasing N, as well as with changes in channel spacing, the relative differences between cable layouts remain similar which is the important result for design optimization. To reduce the effect of variance in the EIG estimate due to the finite number of samples, we use the same set of prior samples for all layout evaluations during the optimization process, since this leads to more consistent relative differences between layouts. These samples are kept constant even for different runs of the optimization process with different random seeds to ensure the best possible comparability between runs. This might lead to a small bias in the results, but our experience from previous studies (D. Strutz & A. Curtis 2024, 2025b) suggests that this effect is small, and the benefits of reduced variance outweigh the potential bias.

We recommend that a small number of hand-chosen layouts are tested before optimization and a range of layouts with different EIG should be evaluated after optimization with different N and channel spacings to ensure that their relative order remains the same when these parameters are changed. Although low numbers of N also have trouble resolving the plateau of the EIG for channel spacings substantially below the correlation length, the relative differences between layouts remain similar. This is supported by the findings of T.S. Hudson *et al.* (2025), which suggest that decimation of channels (up to a certain point) has only a small effect on source location accuracy. Choosing N appropriately is important, because the computational cost scales quadratically with N, while it scales only linearly with the number of channels.

The optimization process begins to converge after approximately 500 generations (see Fig. 10), with the best layout show-

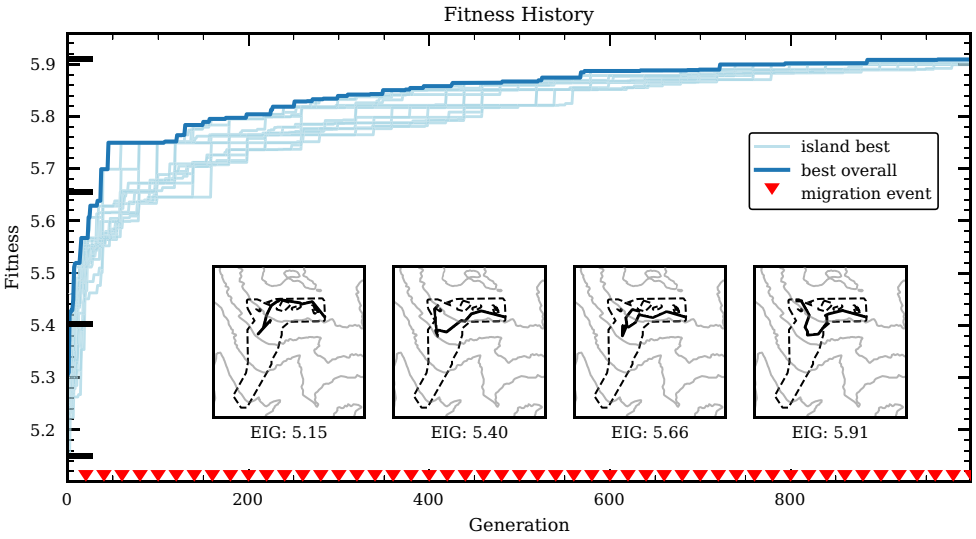

Figure 10. Fitness history of the EIG for the *P*-wave source location design optimization. Shown are both the best layout in the archipelago (dark blue) and the best layout in each island (light blue). The four subplots at the bottom show the cable layouts at different stages of the optimization process (indicated as black bars on the y-axis).

ing a significant improvement in the EIG compared to the initial population. The effect of migrations is clearly visible in the fitness history of individual islands, which prevents some islands from becoming trapped in suboptimal local optima and allows them to contribute to the overall convergence of the optimization process.

While the EIG has beneficial properties for Bayesian design optimization, it lacks a direct intuitive interpretation, which makes the benefits of optimization difficult to appreciate. We therefore present posterior distributions for 10 prior samples in Fig. 11, which shows directly how much better an optimized cable can resolve the source locations. If the collected data provides little information (see right column), the posterior is very similar to the prior.

3.3 Rayleigh wave tomography

To demonstrate the design optimization process for ambient noise tomography, we use Rayleigh waves, as typical sensors deployed on landslides have only a vertical component and are thus most sensitive to Rayleigh waves (M. Le Breton *et al.* 2021; C. Feng *et al.* 2024). The orientation and sensitivity of DAS cables differs inherently from those of typical seismological sensors, with substantial sensitivity to both Rayleigh and Love waves only available when aligned suitably oriented. Our tests show that optimization for Love waves can lead to substantially different layouts, with Rayleigh waves being more sensitive to the cable layout than Love waves.

The design criterion used is D-optimality Σ_D^* ($\lambda_{\text{thr}} = 10^{-4}$, $\lambda_{\text{pen}} = 10\log(10^{-4})$), where the sensitivity matrix is focused (A. Curtis 1999b) to contain only entries relevant to grid cells in the region of interest in the shoulder area (see Fig. 8). The velocity grid is bounded by the envelope of the viable area and has a grid spacing of 20 m. The reference distance is set to 1000 m, which is conservatively low, thus implicitly optimizing for a worst-case scenario in which the signal strength is just sufficient to measure group velocities across the design region at near-perfect alignment. This results in high sensitivity to interchannel orientations.

The optimization history follows a pattern similar to the *P*-wave source location case, with the best layout showing a significant improvement in D-optimality compared to the initial population. Fig. 12 shows the optimal layout, as well as the velocity grid cell sensitivity and selected interchannel ray paths. The figure also includes a checkerboard model used to compute synthetic data using a seismic ray-tracer (B. Giroux 2021), and the results of inverting those data using the sensitivity matrix of both the optimal and the existing DAS cable layout.

The main pattern in the optimal layout is that the cable does not simply wrap around the shoulder region, but features notable angular intrusions. The inter-channel ray paths show that these are likely necessary to enhance the angular sensitivity, since parallel channels provide no sensitivity to the velocity grid cells between them, but they could be equally well explained by the constraint that the cable must be continuous. It is important to note, however, that there are different layouts (albeit showing similar local patterns) that can perform similarly well. This inherent non-uniqueness of the design problem means that multiple distinct layouts can achieve comparable outcomes, provided that they share key features that increase sensitivity, such as appropriate channel orientations and adequate coverage of the area of interest.

3.4 Multi-objective design optimization

To demonstrate the multi-objective design optimization process we optimize the cable layout for both *P*-wave source location and Rayleigh wave tomography simultaneously using the non-dominated sorting genetic algorithm (K. Deb *et al.* 2000).

In a multi-objective optimization process, there is no single optimal solution, but rather a set of optimal solutions known as the Pareto front. Solutions on the Pareto front represent optimal trade-offs between competing objectives, where improved performance in one criterion necessarily requires reduced performance in another. The Pareto front of the final population (and of previous generations) is shown in Fig. 13.

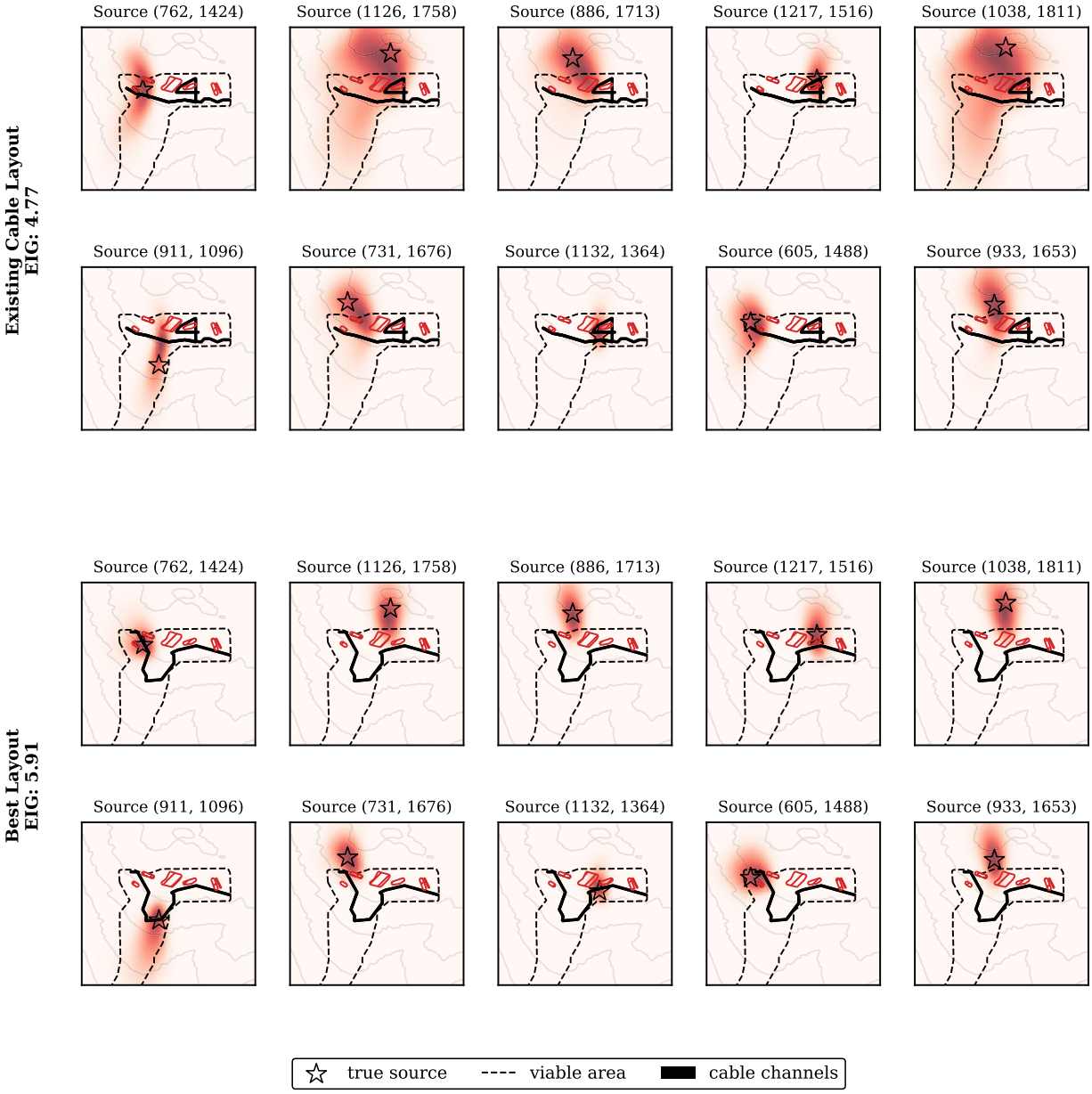

Figure 11. Posterior distributions of the *P*-wave source locations for 10 prior samples (reordered for visualization purposes). The posterior distributions are obtained by calculating the posterior probabilities on a grid with a spacing of 20 m, and marginalizing over the vertical axis. The top and bottom rows show the results for the existing and optimized cable layouts, respectively.

We note that the end-member designs are similar in layout and slightly worse in performance compared to layouts optimised for a single objective. This is an expected outcome, as the multi-objective optimization process aims to improve performance along the entire Pareto front, not just at the end-member designs. During the optimization process, the number of designs on the Pareto front tends to increase as the design space is explored and new designs are found that improve performance in one or both criteria. This provides an increasingly large set of designs from which to choose. Practitioners can select an operating point from the Pareto front using various approaches, such as knee-point detection to identify regions of diminishing returns (J. Branke *et al.* 2004), normalizing objectives to a common utility scale (K. Miettinen 1999) or incorporating soft penalties for practical constraints such as installation cost.

In this specific case, the EIG criterion appears more robust to the particular layout chosen and consistently leads to good (EIG $\geq$ 4.0) performance, whereas the D-optimality criterion is more sensitive to the layout and may result in designs with low D-optimality. This can be explained by the dependence on two channel azimuths and the large model parameter space for Rayleigh wave tomography.

The multi-objective optimization process is flexible and does not require the quantities being optimized to be design performance criteria. For example, we can use the cable length as an objective to be minimized while maximizing the performance

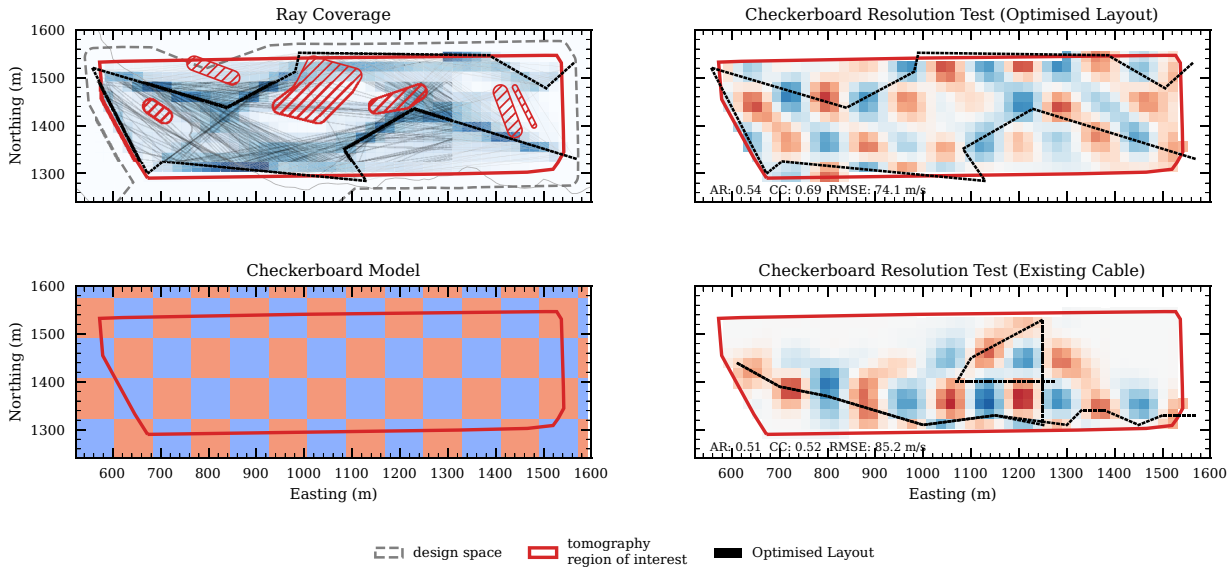

Figure 12. Analysis of the optimal layout for Rayleigh wave tomography. The top left plot shows the sensitivity to velocity grid cells as a heatmap (dark blue indicates high sensitivity, light blue low sensitivity), along with a subset of interchannel ray paths (grey lines). The checkerboard models used for illustration of tomographic quality is shown bottom-left. The top right plot shows the inverted checkerboard model (red indicates high velocity, blue low velocity) that uses the sensitivity matrix of the optimal layout. The bottom right plot shows the inverted checkerboard model for the existing DAS cable layout. Each black rectangle represents a channel and its direction, which is determined by the local direction of the cable. At the bottom of each checkerboard result, common resolution metrics are provided: (AR): amplitude recovery (higher is better), (CC): correlation coefficient (higher is better) and (RMSE): root mean square error (lower is better).

of Rayleigh wave tomography, which leads to a Pareto front that shows the trade-off between cable length and D-optimality (Fig. 14). The maximum possible length of the cable has been increased to 4000 m to allow for longer layouts, and the number of knots has been increased to 16 to allow for more complex layouts.

As expected, cable length is a strong indicator of performance, with longer cables generally providing better results. The cable shapes suggest that the number of knots is more than sufficient for the shorter cables and just adequate for the longer ones. If the range of cable lengths is too wide, we therefore recommend either using a conservatively high number of knots, at the expense of convergence speed, or running several optimization runs for different cable length ranges, each with a different number of knots.

4 DISCUSSION

The DAS layout optimization process presented here is a flexible and scalable approach to design optimization for a wide range of DAS applications. While we have demonstrated the process only for a few specific applications, it can be adapted to any application where the design goal(s) can be expressed quantitatively. The main effort for the practitioner is to specify the prior knowledge necessary, to formulate the design criteria, define the optimization constraints for the cable layout and choose proposal layouts.

The choice of prior knowledge is crucial in any experimental design process (X. Huan *et al.* 2024). Introducing unreasonably strong prior knowledge may bias the design towards specific solutions, while overly weak prior knowledge may lead to designs that attempt to cover a wide range of possible scenarios without focusing on those that occur in practice. Both criteria introduced here allow prior knowledge to be incorporated in a probabilistic way, which enables prior uncertainty to be encoded to some extent. If the practitioner is uncertain about the effect of prior knowledge, they can run a multi-objective optimization to study the effects and trade-offs of different choices. A common example of such a choice is to decide how to fix the velocity model; once chosen, this is straightforward to incorporate (at higher computational cost) and different models can lead to different designs.

All of the presented design criteria can be evaluated within seconds to minutes (on a single CPU core), depending on the exact choices and number of channels. This allows for human-in-the-loop optimization, where the practitioner could interactively change the knot locations and other parameters and immediately see the effects on the design criteria. This is especially useful for complex scenarios where the practitioner has a good understanding of the problem but may not be able to express it fully quantitatively. The use of proposal layouts allows sequential refinement of layouts and incorporation of prior knowledge as well as lessons learned in previous optimization runs. It also allows for sequential increases in the number of knot points and, therefore, the complexity of the design.

While evolutionary algorithms are flexible and scalable, they often require a large number of evaluations to converge to a solution. For computationally expensive applications, such as full waveform and high-dimensional traveltime tomography (H. Maurer *et al.* 2017), this will result in prohibitively long optimization times, even when both the criterion evaluation and the optimization process are parallelized. An efficient alternative to evolutionary algorithms is stochastic gradient descent (SGD) (e.g. A. Foster *et al.* 2020; S. Kleinegesse & M.U. Gutmann 2021). However, SGD requires that both the design criterion and the mapping from knots to channels are differentiable. It is also unclear how design constraints can be incorporated into the optimization process, as SGD is not designed to handle constraints.

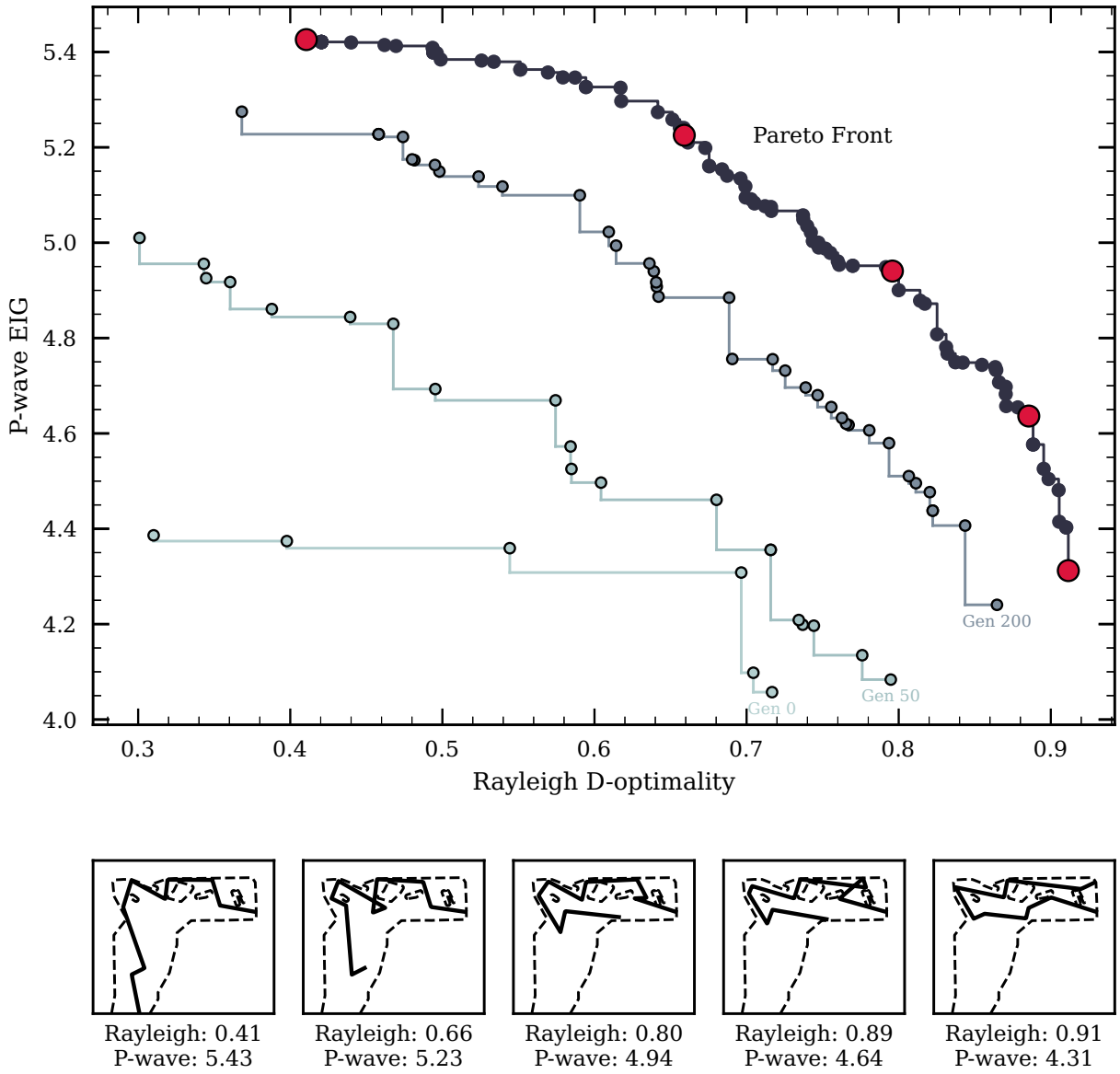

Figure 13. Pareto front of the archipelago population for the final (black) and previous (grey) generations of the multi-objective (*P*-wave source location and Rayleigh wave tomography) design optimization process. Connecting lines are for visualization only. Five selected layouts (red points) are shown with a solid black line in individual plots at the bottom.

The total CPU hours required for the *P*-wave source location and Rayleigh wave tomography examples in Section 3.2 and 3.3 are 133 and 145 hr, respectively. These times correspond to wall-clock times of approximately 8–9 hr when using 16 CPU cores in parallel. The number of CPU hours required depends strongly on the number of channels, the complexity of the design criterion, the number of knots, the population size and the number of generations. While this is still relatively affordable, the two criteria used here are computationally inexpensive to evaluate. For applications that require more expensive forward models, or have high-dimensional model parameter spaces, the computational cost will increase substantially. In such cases, surrogate models, such as Gaussian processes (A.M. Overstall & D.C. Woods 2017) or neural network surrogates (J. Blank & K. Deb 2021), can support the optimization process by providing fast approximations of the design criteria, while multi-fidelity approaches (T.E. Coons & X. Huan 2025) can reduce the computational cost of individual evaluations by using cheaper approximations of the design criteria (coarse grids or simplified criteria) early in the optimization process, and full criteria near the Pareto front.

There are, however, limitations to the current DAS cable parametrization and optimization process. Placing channels at fixed intervals along the spline can result in channels that span sharp bends or kinks in the cable path. Because channel measurements represent averages over a finite gauge length, this may violate the point receiver assumption that underlies our analysis. Although this effect is unlikely to affect the optimization significantly for applications at the scale considered here, it could be mitigated by either excluding affected channels from the analysis, subdividing them into smaller segments with appropriately increased noise levels, or integrating the

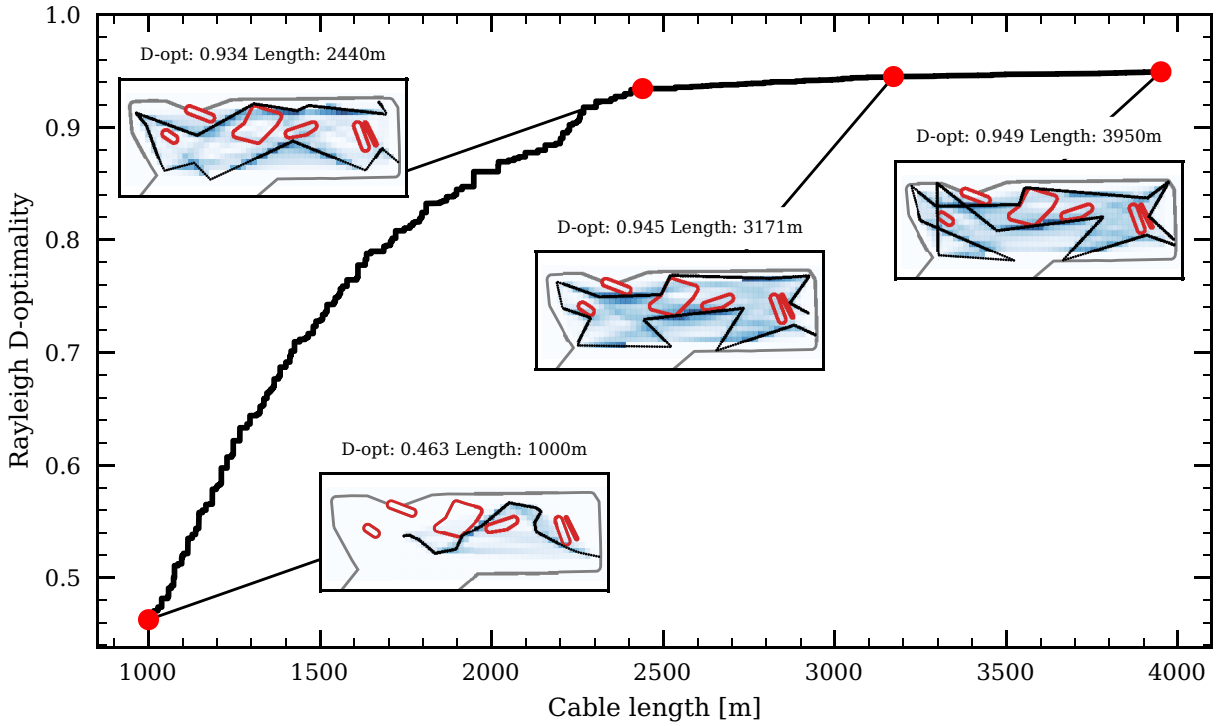

Figure 14. Pareto front of the multi-objective design optimization process for cable length and Rayleigh wave tomography performance. Note that cable length is minimized rather than maximized, which flips the shape of the front compared to Fig. 13. Four selected designs (red dots) are shown along the front, where the solid black line indicates the design and the blue heatmap shows the Rayleigh wave sensitivity.

sensitivity kernel along the gauge length of each channel. For splines of degree $k \geq 1$, it is important to ensure that the channel spacing is sufficiently small so that the effects of curvature remain negligible. The optimization process presented can be extended, given the appropriate sensitivity models, to special cable geometries, such as helically wound cables (K. Innanen 2017; I.L.C. Ning & P. Sava 2018), by replacing the current sensitivity kernels with appropriate models for such geometries. The flexibility of evolutionary algorithms would additionally allow the placement of diverse cable winding patterns as point sensors along the cable. In both cases care needs to be taken to scale the signal-to-noise ratio appropriately. These extensions would typically reduce or totally remove the directional sensitivity and would therefore likely lead to different optimal cable layouts that might, for example, follow more closely what is expected from traditional three-component sensors, while still being restricted by an along-cable layout. In the same way, the genetic optimization process could be adapted to optimise at which end of the cable the interrogator unit is placed, and, if in-line amplifiers are available, where they should be placed along the cable to improve the signal-to-noise ratio.

Another limitation of the current design optimization process is that random crossover and mutation can struggle to respect design constraints, particularly when the viable area is small relative to the cable length or when numerous knots describe the design. This can result in many rejected layouts, which consequently slows convergence. While it remains unclear how to address this issue in general, the crossover and mutation operators could be adapted to reflect design constraints more accurately when generating new layouts.

While it has not been demonstrated in the examples presented here, the two design criteria presented, and the associated code suite, allow for the inclusion of site terms K_i, which can be used to account for channel-specific noise levels, coupling and local signal amplification or attenuation effects. While the inclusion of such factors is straightforward in theory, unless data is available to estimate them (e.g. J. Yin *et al.* 2023), how to accurately estimate them ahead of deployment remains an open question. If substantial variations are expected within the viable area, we recommend construction of a best-guess map of K_i values that describes the local conditions, and use of these values during the design optimization process. Such a map can be constructed either by relying on prior studies in similar environments (e.g. I. Lior *et al.* 2021; J. Yin *et al.* 2023), or by use of synthetic models to estimate likely coupling variations based on surface conditions (e.g. N.L. Celli *et al.* 2023). In such a sensitivity map, the practitioner would also need to decide ahead of time whether a cable is buried or not, depending on the location.

Finally, although we have focused on the design of single DAS cables only, the design optimization process can be straightforwardly adapted to hybrid (e.g. DAS and geophone) or multi-cable scenarios due to the inherent flexibility of evolutionary algorithms. In this case a set number of additional optimization variables would be introduced which do not describe cable anchors but instead the locations of additional sensors. Those sensors can of course be constrained in similarly to the cable knots (e.g. restricted areas). The design criteria would then need to be adapted to account for the different sensor types and their noise levels. We have omitted this from the present study, as combining data from different sensor types is a non-trivial task (T.S. Hudson *et al.* 2025). If estimates for noise levels (and coupling) of different sensor types are available, the reference distance can be replaced by a source magnitude for which the hybrid design can be optimised. If the additional stations are in a

low-noise environment, one could also assume that these stations record every signal (independent of distance and direction) and proceed with a reference distance only for the DAS cable as described above.

5 CONCLUSION

This study presents a flexible approach to optimizing DAS cable layouts for geophysical applications. We have developed a parametric representation that uses splines to explore possible layouts efficiently while respecting physical constraints. Our adapted design criteria for source location and surface wave tomography incorporate DAS-specific characteristics such as directional sensitivity and signal decay.

Evolutionary algorithms offer robust optimization capabilities for complex design spaces with multiple constraints, while multi-objective optimization enables the exploration of trade-offs between competing goals. The generalized island model allows parallelization with limited communication overhead, which makes the approach computationally feasible for realistic scenarios.

The Cuolm da Vi slope instability case study demonstrates that optimized DAS layouts significantly improve performance compared to initial designs, with different optimization targets resulting in distinctly different cable geometries. Despite limitations in computational efficiency for very complex models, our framework supports evidence-based decision-making when planning DAS deployments for specific monitoring objectives.

ACKNOWLEDGMENTS

The implementations of the algorithms in this work would not have been possible without extensive use of open-source software. Not all of them have been included in the respective sections to ease readability. All the code was written in Python (G. Van Rossum & F. Drake 2011), PyTorch (A. Paszke *et al.* 2019) was used to process probability distributions and calculate the EIG and Matplotlib (J.D. Hunter 2007) for plotting.

During the preparation of this work the authors used LLMs as a tool in the code development process and as a grammar and spelling checker during the writing process. After using this tool, the authors reviewed and edited the content as needed and take full responsibility for the content of the published article.

This project has received funding from the European Union's Horizon 2020 research and innovation programme under the Marie Skłodowska-Curie grant agreement No 955515–SPIN ITN (www.spin-itn.eu)

DATA AVAILABILITY

This study only uses synthetic data. The algorithms developed in this work are available at https://github.com/dominik-strutz/dased and the code to reproduce the figures is available at https://github.com/dominik-strutz/dased_paper.

REFERENCES

Ajo-Franklin, J.B. *et al.*, 2019. Distributed acoustic sensing using dark fiber for near-surface characterization and broadband seismic event detection, *Sci. Rep.,* **9**(1), 1328.

Aki, K., 1976. Signal to noise ratio in seismic measurements, *Volcanoes and Tectonosphere,* 187–192.

Alexanderian, A., 2021. Optimal experimental design for infinite-dimensional Bayesian inverse problems governed by PDEs: a review, *Inverse Probl.,* **37**(4), 043001..

Alexanderian, A., Nicholson, R. & Petra, N., 2024. Optimal design of large-scale nonlinear Bayesian inverse problems under model uncertainty, *Inverse Probl.,* **40,** 095001.

Amann, F., 2006. Großhangbewegung Cuolm Da Vi (Graubünden, Schweiz)Geologisch-geotechnische Befunde und numerischeUntersuchungen zur Klärung des Phänomens, PhD thesis, Friedrich-Alexander-Universität Erlangen-Nürnberg, https://opus4.kobv.de/opus4-fau/files/283/Amann_Dissertation.pdf. (1 August 2025, date last accessed).

Atkinson, A.C. & Donev, A.N., 1992. *Optimum Experimental Designs, Oxford Statistical Science Series,* Clarendon Press.

Baba, S., Araki, E., Yokobiki, T., Kawamata, K., Uchiyama, K. & Yoshizuka, T., 2024. Seismic observation using distributed acoustic sensing around the Tsugaru Strait at the Japan and Kuril Trenches, northeastern Japan, *Earth Planets Space,* **76**(1), 1–12.

Baird, A.F., Morten, J.P., Oye, V. & Bjørnstad, S., 2025. Ocean space surveillance and real-time event characterization using Distributed acoustic sensing on submarine networks, *Seismol. Res. Lett.,* **96**(2A), 691–705.

Barbour, A.J. & Crowell, B.W., 2017. Dynamic strains for earthquake source characterization, *Seismol. Res. Lett.,* **88**(2A), 354–370.

Barbour, A.J., Langbein, J.O. & Farghal, N.S., 2021. Earthquake magnitudes from dynamic strain, *Bull. seism. Soc. Am.,* **111**(3), 1325–1346..

Ben-Zeev, S. & Lior, I., 2025. Earthquake location with distributed acoustic sensing subarray beamforming with implications for earthquake early warning, *Seismol. Res. Lett.,* **96**(4), 2453–2462.

Biscani, F. & Izzo, D., 2020. A parallel global multiobjective framework for optimization: pagmo, *J. Open Source Softw.,* **5**(53), 2338.

Blank, J. & Deb, K., 2021. PSAF: a probabilistic surrogate-assisted framework for single-objective optimizationin *Proceedings of the Genetic and Evolutionary Computation Conference,* ACM, New York, NY, USA.

Bloem, H., Curtis, A. & Maurer, H., 2020. Experimental design for fully nonlinear source location problems: which method should I choose?, *Geophys. J. Int.,* **223**(2), 944–958..

Box, G.E.P. & Lucas, H.L., 1959. Design of Experiments in Non-Linear Situations, *Biometrika,* **46**(1-2), 77..

Branke, J., Deb, K., Dierolf, H. & Osswald, M., 2004. Finding knees in multi-objective optimization, in *Parallel Problem Solving from Nature - PPSN VIII. PPSN 2004*. Lecture Notes in Computer Science, pp. 722–731, eds Yao, X.et al. Springer. doi: 10.1007/978-3-540-30217-9_73.

Callahan, J., Monogue, K., Villarreal, R. & Catanach, T., 2025. Analysis and optimization of seismic monitoring networks with Bayesian optimal experimental design, *Geophys. J. Int.,* **240**(3), 1802–1824..

Celli, N.L., Bean, C.J. & O'Brien, G., 2023. Full-waveform simulation of DAS records, response, and cable-ground coupling, *Geophys. J. Int.,* **236**(1), 659–674..

Chowdhary, A., Attia, A. & Alexanderian, A., 2024. Robust optimal design of large-scale Bayesian nonlinear inverse problems, preprint(arXiv:[math.NA]).

Coons, T.E. & Huan, X., 2025. A multi-fidelity estimator of the expected information gain for Bayesian optimal experimental design, *SIAM/ASA J. Uncertain. Quantif.,* **13**(4).

Cover, T.M. & Thomas, J.A., 2006. *Elements of Information Theory,* 2nd edn, John Wiley and Sons.

Curtis, A., 1999a. Optimal experiment design: cross-borehole tomographic examples, *Geophys. J. Int.,* **136**(3), 637–650..

Curtis, A., 1999b. Optimal design of focused experiments and surveys, *Geophys. J. Int.,* **139**(1), 205–215..

Curtis, A., 2004a. Theory of model-based geophysical survey and experimental design: Part 2-nonlinear problems, *Leading Edge,* **23**(11), 1112–1117..

Curtis, A., 2004b. Theory of model-based geophysical survey and experimental design: Part 1-linear problems, *Leading Edge,* **23**(10), 997–1004..

Curtis, A. & Snieder, R., 1997. Reconditioning inverse problems using the genetic algorithm and revised parameterization, *Geophysics,* **62**(5), 1524–1532..

Curtis, A., Michelini, A., Leslie, D. & Lomax, A., 2004. A deterministic algorithm for experimental design applied to tomographic and microseismic monitoring surveys, *Geophys. J. Int.,* **157**(2), 595–606..

Curtis, A., Gerstoft, P., Sato, H., Snieder, R. & Wapenaar, K., 2006. Seismic interferometry–turning noise into signal, *Leading Edge,* **25**(9), 1082–1092..

Daley, T.M. *et al.*, 2013. Field testing of fiber-optic distributed acoustic sensing (DAS) for subsurface seismic monitoring, *Leading Edge,* **32**(6), 699–706..

Daley, T.M., Miller, D.E., Dodds, K., Cook, P. & Freifeld, B.M., 2016. Field testing of modular borehole monitoring with simultaneous distributed acoustic sensing and geophone vertical seismic profiles at Citronelle, Alabama: Field testing of MBM, *Geophys. Prospect.,* **64**(5), 1318–1334..

De Boor, C., 2001. *A Practical Guide to Splines,* Applied Mathematical Sciences, 1st edn, Springer.

Deb, K., Agrawal, S., Pratap, A. & Meyarivan, T., 2000. A fast elitist non-dominated sorting genetic algorithm for multi-objective optimization: NSGA-II, in *Parallel Problem Solving from Nature PPSN VI,* Lecture notes in computer science, pp. 849–858, Schoenauer, M.et al., Springer, Berlin, Heidelberg.

Dinh, L., Krueger, D. & Bengio, Y., 2014. NICE: Non-linear independent components estimation, preprint(arXiv:[cs.LG]).

Englezou, Y., Waite, T.W. & Woods, D.C., 2022. Approximate Laplace importance sampling for the estimation of expected Shannon information gain in high-dimensional Bayesian design for nonlinear models, *Stat. Comput.,* **32**(5), 82.

Fang, J. *et al.*, 2023. Directional sensitivity of DAS and its effect on Rayleigh-wave tomography: a case study in Oxnard, California, *Seismol. Res. Lett.,* **94**(2A), 887–897.

Feng, C., Yamaoka, K., Ikuta, R., Watanabe, T. & Tsuji, S., 2024. Surface wave monitoring using ambient noise for detecting temporal variations in underground structures in landslide area, *Eng. Geol.,* **341**(107706), 107706.

Fichtner, A. & Hofstede, C., 2022. A simple algorithm for optimal design in distributed fibre-optic sensing, *Geophys. J. Int.,* **233**(1), 229–233..

Fichtner, A., Klaasen, S., Thrastarson, S., Çubuk Sabuncu, Y., Paitz, P. & Jónsdóttir, K., 2022. Fiber-optic observation of volcanic tremor through floating ice sheet resonance, *The Seismic Record,* **2**(3), 148–155..

Foster, A., Jankowiak, M., Bingham, E., Horsfall, P., Teh, Y., Rainforth, T. & Goodman, N.D., 2019. Variational Bayesian optimal experimental design, *Neur. Inform. Process. Syst.,* **32,** 14 036–14 047.

Foster, A., Jankowiak, M., O'Meara, M., Teh, Y.W. & Rainforth, T., 2020. A unified stochastic gradient approach to designing Bayesian-optimal experiments, *International Conference on Artificial Intelligence and Statistics,* PMLR.

Fuggi, A., Re, S., Tango, G., Del Gaudio, S., Brovelli, A. & Cassiani, G., 2024. Assessment of earthquake location uncertainties for the design of local seismic networks, *Earthq. Sci.,* **37**(5), 415–433.

Gad, A.G., 2022. Particle swarm optimization algorithm and its applications: a systematic review, *Arch. Computat. Methods Eng.,* State of the Art Reviews, **29**(5), 2531–2561.

Giroux, B., 2021. ttcrpy: A Python package for traveltime computation and raytracing, *SoftwareX,* **16**(100834), 100834..

Golub, G.H. & Van Loan, C.F., 2013. *Matrix Computations,* Johns Hopkins Studies in the Mathematical Sciences, 4th edn, Johns Hopkins University Press.

Guest, T. & Curtis, A., 2010. Optimal trace selection for AVA processing of shale-sand reservoirs, *Geophysics,* **75**(4), C37–C47..

Holland, J.H., 1984. Genetic algorithms and adaptation, in *Adaptive Control of Ill-Defined Systems,* pp. 317–333, eds Selfridge, O.G., Rissland, E.L. & Arbib, M.A., Springer US.

Holland, J.H., 2021. Adaptation in Natural and Artificial Systems. Available at: https://mitpress.mit.edu/9780262581110/adaptation-in-natural-and-artificial-systems/, Accessed: 2025-8-1.

Huan, X. & Marzouk, Y.M., 2013. Simulation-based optimal Bayesian experimental design for nonlinear systems, *J. Comput. Phys.,* **232**(1), 288–317.

Huan, X., Jagalur, J. & Marzouk, Y., 2024. Optimal experimental design: Formulations and computations, *Acta Numer.,* **33,** 715–840.

Hudson, T.S. *et al.*, 2021. Distributed acoustic sensing (DAS) for natural microseismicity studies: A case study from Antarctica, *J. geophys. Res.. Solid earth,* **126**(7), e2020JB021493..

Hudson, T.S., Klaasen, S., Fontaine, O., Bacon, C.A., Jónsdóttir, K. & Fichtner, A., 2025. Towards a widely applicable earthquake detection algorithm for fibreoptic and hybrid fibreoptic-seismometer networks, *Geophys. J. Int.,* **240**(3), 1965–1985..

Hunter, J.D., 2007. Matplotlib: A 2D Graphics Environment, *Comput. Sci. Eng.,* **9**(3), 90–95.

Hutton, L.K. & Boore, D.M., 1987. The*ML*scale in southern California, *Bull. seism. Soc. Am.,* **77**(6), 2074–2094..

Innanen, K., 2017. Determination of seismic-tensor strain from Helical Wound Cable-Distributed Acoustic Sensing cable with arbitrary and nested-helix winds in SEG Technical Program Expanded Abstracts 2017, Society of Exploration Geophysicists, 926–930.

Izzo, D., Ruciński, M. & Biscani, F., 2012. The generalized island model, in *Parallel Architectures and Bioinspired Algorithms, Studies in computational intelligence,* pp. 151–169, Springer.

Jousset, P. *et al.*, 2022. Fibre optic distributed acoustic sensing of volcanic events, *Nat. Commun.,* **13**(1), 1753.

Kennett, B.L.N., 2024. *A Guide to the Seismic Wavefield as seen by DAS,* The Australian National University.

Kiers, T., Schmelzbach, C., Maurer, H., Amann, F. & Robertsson, J., 2026a. Imaging one of the largest Alpine slope instabilities with 3D seismic first-arrival traveltime tomography, *J. Appl. Geophy.,* **247,** 106081.

Kiers, T., Schmelzbach, C., Amann, F., Maurer, H., Edme, P., Rinaldi, A., Bonanomi, Y. & Robertsson, J., 2026b. Advancing seismic slope instability monitoring: integrating fibre-optic and nodal array sensing, *Seismica [Accepted]*. Doi:10.26443/seismica.v5i1.1997.

Kijko, A., 1977a. An algorithm for the optimum distribution of a regional seismic network–I, *Pure appl. Geophys.,* **115**(4), 999–1009..

Kijko, A., 1977b. An algorithm for the optimum distribution of a regional seismic network–II. An analysis of the accuracy of location of local earthquakes depending on the number of seismic stations, *Pure appl. Geophys.,* **115**(4), 1011–1021..

Klaasen, S., Paitz, P., Lindner, N., Dettmer, J. & Fichtner, A., 2021. Distributed acoustic sensing in volcano-glacial environments–Mount Meager, British Columbia, *J. geophys. Res.. Solid earth,* **126**(11)..

Kleinegesse, S. & Gutmann, M.U., 2021. Gradient-based Bayesian experimental design for implicit models using mutual information lower bounds, preprint(arXiv:2105.04379).

Krampe, V., Edme, P. & Maurer, H., 2021. Optimized experimental design for seismic full waveform inversion: a computationally efficient method including a flexible implementation of acquisition costs, *Geophys. Prospect.,* **69**(1), 152–166..

Kuvshinov, B.N., 2016. Interaction of helically wound fibre-optic cables with plane seismic waves: interaction of fibre-optic cables, *Geophys. Prospect.,* **64**(3), 671–688..

Le Breton, M., Bontemps, N., Guillemot, A., Baillet, L. & Larose, É., 2021. Landslide monitoring using seismic ambient noise correlation: challenges and applications, *Earth-Sci. Rev.,* **216**(103518), 103518..

Li, L., Boué, P., Retailleau, L. & Campillo, M., 2020. Spatiotemporal correlation analysis of noise-derived seismic body waves with ocean wave climate and microseism sources, *Geochem. Geophys. Geosyst.: G(3),* **21**(9), e2020GC009112..

Lindley, D.V., 1956. On a measure of the information provided by an experiment, *Ann. Math. Stat.,* **27**(4), 986–1005.
Lindsey, N.J. & Martin, E.R., 2021. Fiber-optic seismology, *Annu. Rev. Earth planet. Sci.,* **49**(1), 309–336.
Lindsey, N.J., Martin, E.R., Dreger, D.S., Freifeld, B., Cole, S., James, S.R., Biondi, B.L. & Ajo-Franklin, J.B., 2017. Fiber-optic network observations of earthquake wavefields: Fiber-optic earthquake observations, *Geophys. Res. Lett.,* **44**(23), 11792–11799..
Lior, I. *et al.*, 2021. On the detection capabilities of underwater distributed acoustic sensing, *J. geophys. Res.. Solid earth,* **126**(3), e2020JB020925..
Lior, I., Rivet, D., Ampuero, J.P., Sladen, A., Barrientos, S., Sánchez-Olavarría, R., Villarroel Opazo, G.A. & Bustamante Prado, J.A., 2023. Magnitude estimation and ground motion prediction to harness fiber optic distributed acoustic sensing for earthquake early warning, *Sci. Rep.,* **13**(1), 424..
Long, Q., Motamed, M. & Tempone, R., 2015. Fast Bayesian optimal experimental design for seismic source inversion, *Comput. Methods Appl. Mech. Eng.,* **291,** 123–145..
Luckie, T. & Porritt, R., 2024. Performance of synthetic DAS as a function of array geometry, *Seismica,* **3**(2), doi: 10.26443/seismica.v3i2.1146.
Martin, E.R., Fabien-Ouillet, G., Clapp, R.G. & Biondo, B., 2017. Sensitivity analysis of distributed acoustic sensing arrays, *Stanford Explor. Rep.,* **170,** 57–80.
Martin, E.R., Lindsey, N.J., Ajo-Franklin, J.B. & Biondi, B.L., 2021. *Introduction to Interferometry of Fiber-optic Strain Measurements,* American Geophysical Union.
Masoudi, A., Beresna, M. & Brambilla, G., 2021. 152 km-range single-ended distributed acoustic sensor based on inline optical amplification and a micromachined enhanced-backscattering fiber, *Optics letters,* **46**(3), 552–555..
Mateeva, A. *et al.*, 2014. Distributed acoustic sensing for reservoir monitoring with vertical seismic profiling: Distributed acoustic sensing (DAS) for reservoir monitoring with VSP, *Geophys. Prospect.,* **62**(4), 679–692..
Maurer, H. & Boerner, D.E., 1998. Optimized design of geophysical experiments, *Leading Edge,* **17**(8), 1119–1119..
Maurer, H., Greenhalgh, S. & Latzel, S., 2009. Frequency and spatial sampling strategies for crosshole seismic waveform spectral inversion experiments, *Geophysics,* **74**(6), WCC79–WCC89..
Maurer, H., Curtis, A. & Boerner, D.E., 2010. Recent advances in optimized geophysical survey design, *Geophysics,* **75**(5), 75A177–75A194..
Maurer, H., Nuber, A., Korta Martiartu, N., Reiser, F., Boehm, C., Manukyan, E., Schmelzbach, C. & Fichtner, A., 2017. Optimized experimental design in the context of seismic full waveform inversion and seismic waveform imaging, in *Advances in Geophysics, vol. 58 of Advances in geophysics,* pp. 1–45, ed. Lars, N., Elsevier.
Menke, W., 2018. *Geophysical Data Analysis: Discrete Inverse Theory,* Academic Press.
Mercier, A., Boehm, C. & Maurer, H., 2025. Designing full waveform inverse problems: a combined data and model approach, *Geophys. J. Int.,* **241**(3), 1479–1494..
Miao, Y., Salaree, A., Spica, Z.J., Nishida, K., Yamada, T. & Shinohara, M., 2025. Assessing the earthquake recording capability of an ocean-bottom distributed acoustic sensing array in the Sanriku region, Japan, *Seismol. Res. Lett.,* **96**(2A), 631–650.
Miettinen, K., 1999. *Nonlinear Multiobjective Optimization,* Kluwer Academic Publishers.
Murphy, K.P., 2022. *Probabilistic Machine Learning: An Introduction,* The MIT Press.
Näsholm, S.P., Iranpour, K., Wuestefeld, A., Dando, B.D.E., Baird, A.F. & Oye, V., 2022. Array signal processing on distributed acoustic sensing data: directivity effects in slowness space, *J. geophys. Res.. Solid earth,* **127**(2), e2021JB023587. doi: 10.1029/2021JB023587.
Ning, I.L.C. & Sava, P., 2018. High-resolution multi-component distributed acoustic sensing: Hi-res multi-component DAS, *Geophys. Prospect.,* **66**(6), 1111–1122..
Overstall, A.M. & Woods, D.C., 2017. Bayesian design of experiments using approximate coordinate exchange, *Technometrics*: a journal of statistics for the physical, chemical, and engineering sciences, **59**(4), 458–470.
Pablo Canales, J., Collins, J.A., Escartín, J. & Detrick, R.S., 2000. Seismic structure across the rift valley of the Mid-Atlantic Ridge at 23°20' (MARK area): Implications for crustal accretion processes at slow spreading ridges, *J. geophys. Res.: Solid Earth,* **105**(B12), 28 411–28 425.
Paszke, A. *et al.*, 2019. PyTorch: An imperative style, high-performance deep learning library, in *Proc. 33rd International Conference on Neural Information Processing Systems,* pp. 8026–-8037, Association for Computing Machinery.
Rabinowitz, N. & Steinberg, D.M., 1990. Optimal configuration of a seismographic network: A statistical approach, *Bull. seism. Soc. Am.,* **80**(1), 187–196..
Ryan, K.J., 2003. Estimating expected information gains for experimental designs with application to the random fatigue-limit model, *J. Comput. Graph. Stat.*: a joint publication of American Statistical Association, Institute of Mathematical Statistics, Interface Foundation of North America, **12**(3), 585–603.
Schweitzer, J., Fyen, J., Mykkeltveit, S., Gibbons, S.J., Pirli, M., Kühn, D. & Kværna, T., 2012. Seismic arrays, in *New manual of seismological observatory practice 2 (NMSOP-2),* pp. 1–80, Deutsches GeoForschungsZentrum GFZ.
Shannon, C.E., 1948. A mathematical theory of communication, *Bell Syst. Techn. J.,* **27**(3), 379–423..
Shapiro, N.M., Campillo, M., Stehly, L. & Ritzwoller, M.H., 2005. High-resolution surface-wave tomography from ambient seismic noise, *Science (New York, N.Y.),* **307**(5715), 1615–1618..
Snieder, R., 2004. Extracting the Green's function from the correlation of coda waves: a derivation based on stationary phase, *Phys. Rev. E*(Statistical, nonlinear, and soft matter physics) **69**(4), 046610.
Spica, Z.J., Perton, M., Martin, E.R., Beroza, G.C. & Biondi, B., 2020. Urban seismic site characterization by fiber-optic seismology, *J. geophys. Res.. Solid earth,* **125**(3), e2019JB018656
Steinberg, D.M., Rabinowitz, N., Shimshoni, Y. & Mizrachi, D., 1995. Configuring a seismographic network for optimal monitoring of fault lines and multiple sources, *Bull. seism. Soc. Am.,* **85**(6), 1847–1857..
Storn, R. & Price, K., 1997. Differential evolution–A simple and efficient heuristic for global optimization over continuous spaces, *J. Global Optim.*(an international journal dealing with theoretical and computational aspects of seeking global optima and their applications in science, management and engineering) **11**(4), 341–359.
Strutz, D. & Curtis, A., 2024. Variational Bayesian experimental design for geophysical applications: seismic source location, amplitude versus offset inversion, and estimating CO_2 saturations in a subsurface reservoir, *Geophys. J. Int.,* **236**(3), 1309–1331..
Strutz, D. & Curtis, A., 2025a. Near-real-time design of experiments for seismic monitoring of volcanoes, *Seismica,* **4**(1), doi: 10.26443/seismica.v4i1.1452.
Strutz, D. & Curtis, A., 2025b. The roles of low-noise stations, arrays and ocean-bottom seismometers in monitoring UK offshore seismicity associated with subsurface storage of carbon dioxide, *Int. J. Greenhouse Gas Control,* **148**(104536), 104536..
Tabak, E.G. & Turner, C.V., 2013. A family of nonparametric density estimation algorithms, *Commun. Pure Appl. Math.,* **66**(2), 145–164.
Tarantola, A. & Valette, B., 1982. Inverse problems = Quest for information, *J. Geophys.,* **50**(1), 159–170.
Thrastarson, S., Torfason, R., Klaasen, S., Paitz, P., Cubuk Sabuncu, Y., Jónsdóttir, K. & Fichtner, A., 2021. Detecting seismic events with computer vision: applications for fiber-optic sensing, *Earth Space Sci. Open Archive*.
Van Rossum, G. & Drake, F., 2011. *The Python Language Reference Manual,* Network Theory.
Vikhar, P.A., 2016. Evolutionary algorithms: a critical review and its future prospects, in *2016 International Conference on Global*

Trends in Signal Processing, Information Computing and Communication (ICGTSPICC), pp. 261–265, IEEE. doi: 10.1109/ICGTSPICC35210.2016.

Virtanen, P. *et al.*, 2020. SciPy 1.0: fundamental algorithms for scientific computing in Python, *Nat. Methods,* **17**(3), 261–272.

Walter, F., Gräff, D., Lindner, F., Paitz, P., Köpfli, M., Chmiel, M. & Fichtner, A., 2020. Distributed acoustic sensing of microseismic sources and wave propagation in glaciated terrain, *Nat. Commun.,* **11**(1), 2436.

Westbrook, P.S. *et al.*, 2020. Enhanced optical fiber for distributed acoustic sensing beyond the limits of Rayleigh backscattering, *iScience,* **23**(6), 101137..

Wu, K., Chen, P. & Ghattas, O., 2023a. An offline-online decomposition method for efficient linear Bayesian goal-oriented optimal experimental design: Application to optimal sensor placement, *SIAM J. Sci. Comput.*(a publication of the Society for Industrial and Applied Mathematics) **45**(1), B57–B77.

Wu, K., Chen, P. & Ghattas, O., 2023b. A fast and scalable computational framework for large-scale high-dimensional Bayesian optimal experimental design, *SIAM/ASA J. Uncertainty Quant.,* **11**(1), 235–261.

Wu, K., O'Leary-Roseberry, T., Chen, P. & Ghattas, O., 2023x. Large-scale Bayesian optimal experimental design with derivative-informed projected neural network, *J. Sci. Comput.,* **95**(1), 30.

Yang, Y., Atterholt, J.W., Shen, Z., Muir, J.B., Williams, E.F. & Zhan, Z., 2022. Sub-kilometer correlation between near-surface structure and ground motion measured with distributed acoustic sensing, *Geophys. Res. Lett.,* **49**(1), e96503..

Yin, J. *et al.*, 2023. Earthquake magnitude with DAS: a transferable data-based scaling relation, *Geophys. Res. Lett.,* **50**(10), e2023GL103045.

Zelt, C.A. & Forsyth, D.A., 1994. Modeling wide-angle seismic data for crustal structure: Southeastern Grenville Province, *J. geophys. Res.: Solid Earth,* **99**(B6), 11 687–11 704..

APPENDIX A: OPTIMIZATION BENCHMARKS

In this section we show how the cable parametrization and the main optimization parameters affect the performance of the optimization algorithm. For this we use the Rayleigh wave tomography setup from Section 3.3.

The number of knots N_{knot} and spline degree k determine which shapes the DAS cable can take. A larger number of knots allows for more complex shapes, but also increases the number of parameters to be optimized. The spline degree k determines the continuity of the cable shape, with higher values leading to smoother shapes. In Fig. A1 we show that an increase in N_{knot} leads to initially better fitness, but after about ten knots the returns diminish. A linear spline ($k = 1$) performs slightly better than a cubic spline ($k = 3$) for the same number of knots, with the difference becoming less pronounced for larger N_{knot}. Therefore we use a linear spline with ten knots in this paper. While using more knots seems like a safer choice, convergence during optimization is slower in the cases we tested (see results for more than fifteen knots in Fig. A1, which perform increasingly poorly). It is also harder to generate a good initial population for larger N_{knot}, since the random perturbation leads to a jagged cable that covers less distance than one with fewer knots. This can be alleviated by the use of correlated permutations, which artificially smooth the cable shape.

The population size N_{pop} determines how many candidate solutions are evaluated in each generation. A larger population size allows for more exploration of the parameter space, but also increases the computational cost. The migration step-size N_{migrate} determines how often solutions are exchanged between islands. If migrations occur too frequently, the diversity across islands is reduced, which can lead to convergence to a local optimum. If migrations occur too infrequently, the islands may not share good solutions, which can lead to slower convergence. In Fig. A2 we show that a large population size is the main factor in improving the fitness and making it more consistent across optimization runs. The migration step-size has a smaller effect, with a migration every 5–20 generations leading to the best results if the population size is sufficiently large. Migration every generation leads to the worst results, which shows the benefits of separate islands compared to one large population.

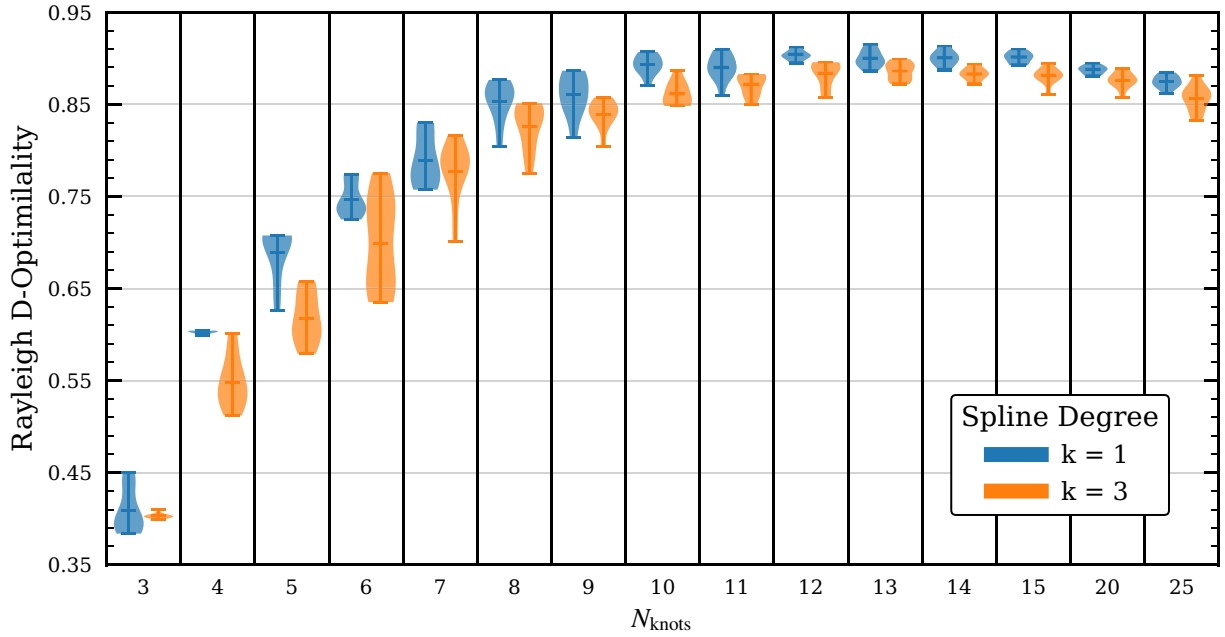

Figure A1. The effect of the number of knots N_{knot} and spline degree k on the fitness of the optimized cable shape. The violin plots show the distribution of fitness values for each combination of N_{knot} and k, for five optimization runs with different random seeds.

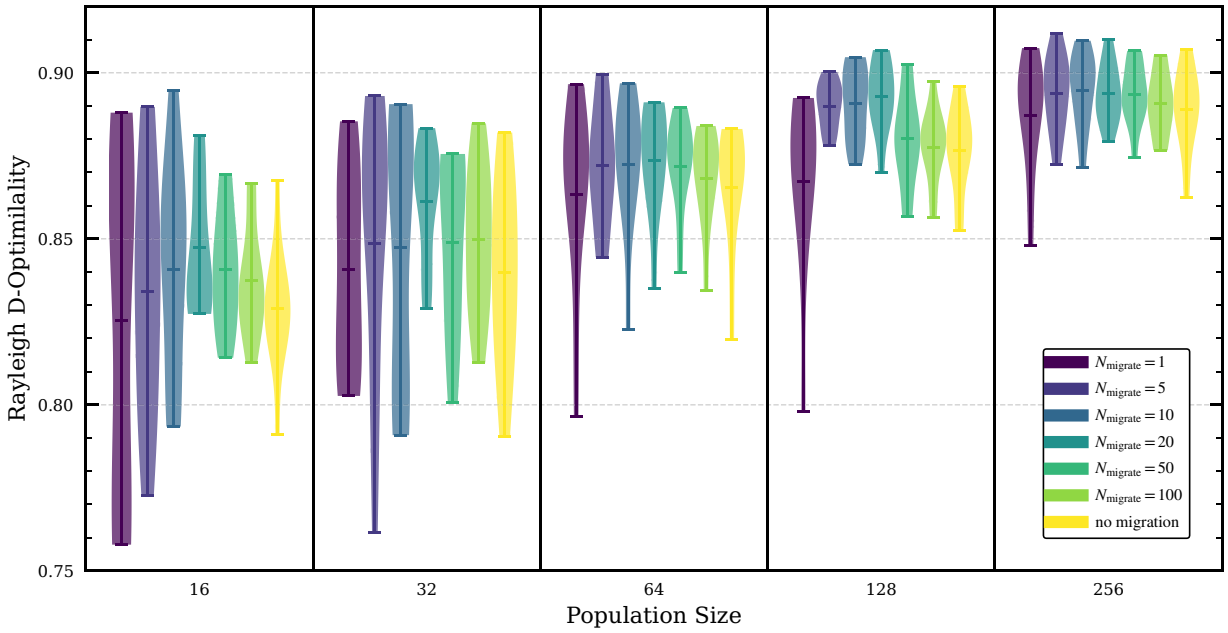

Figure A2. The effect of the population size N_{pop} and migration step-size N_{migrate} on the fitness of the optimized cable shape. The violin plots show the distribution of fitness values for each combination of N_{pop} and N_{migrate} for five optimization runs with different random seeds.